AGU PUBLICATIONS

JGR

Journal of Geophysical Research: Oceans

RESEARCH ARTICLE

10.1002/2017JC012923

Special Section:
The Southern Ocean Carbon and Climate Observations and Modeling (SOCCOM) Project: Technologies, Methods, and Early Results

Oxygen in the Southern Ocean From Argo Floats: Determination of Processes Driving Air-Sea Fluxes

Seth M. Bushinsky[1], Alison R. Gray[1,2], Kenneth S. Johnson[3], and Jorge L. Sarmiento[1]

[1]Atmospheric and Oceanic Sciences, Princeton University, Princeton, NJ, USA, [2]Now at School of Oceanography, University of Washington, Seattle, WA, USA, [3]Monterey Bay Aquarium Research Institute, Moss Landing, CA, USA

Abstract The Southern Ocean is of outsized significance to the global oxygen and carbon cycles with relatively poor measurement coverage due to harsh winters and seasonal ice cover. In this study, we use recent advances in the parameterization of air-sea oxygen fluxes to analyze 9 years of oxygen data from a recalibrated Argo oxygen data set and from air-calibrated oxygen floats deployed as part of the Southern Ocean Carbon and Climate Observations and Modeling (SOCCOM) project. From this combined data set of 150 floats, we find a total Southern Ocean oxygen sink of -183 ± 80 Tmol yr^{-1} (positive to the atmosphere), greater than prior estimates. The uptake occurs primarily in the Polar-Frontal Antarctic Zone (PAZ, -94 ± 30 Tmol O_2 yr^{-1}) and Seasonal Ice Zone (SIZ, -111 ± 9.3 Tmol O_2 yr^{-1}). This flux is driven by wintertime ventilation, with a large portion of the flux in the SIZ passing through regions with fractional sea ice. The Subtropical Zone (STZ) is seasonally driven by thermal fluxes and exhibits a net outgassing of 47 ± 29 Tmol O_2 yr^{-1} that is likely driven by biological production. The Subantarctic Zone (SAZ) uptake is -25 ± 12 Tmol O_2 yr^{-1}. Total oxygen fluxes were separated into a thermal and nonthermal component. The nonthermal flux is correlated with net primary production and mixed layer depth in the STZ, SAZ, and PAZ, but not in the SIZ where seasonal sea ice slows the air-sea gas flux response to the entrainment of deep, low-oxygen waters.

Key Points:
- Determination of large oxygen sink in the Southern Ocean from newly available Argo oxygen data
- This sink is primarily due to wintertime uptake in the regions south of the Subantarctic Front and in water seasonally covered by ice
- The Subtropical Southern Ocean is a net source of biologically produced oxygen, while ventilation to the south drives uptake

Supporting Information:
- Supporting Information S1

Correspondence to:
S. M. Bushinsky,
sb17@princeton.edu

Citation:
Bushinsky, S. M., Gray, A. R., Johnson, K. S., & Sarmiento, J. L. (2017). Oxygen in the Southern Ocean from Argo floats: Determination of processes driving air-sea fluxes. *Journal of Geophysical Research: Oceans*, *122*, 8661–8682. https://doi.org/10.1002/2017JC012923

Received 26 MAR 2017
Accepted 10 OCT 2017
Accepted article online 15 OCT 2017
Published online 12 NOV 2017

© 2017. American Geophysical Union. All Rights Reserved.

1. Introduction

Changes to the oxygen cycle are a predicted consequence of global warming, due to the temperature dependence of saturation and expected changes in ventilation from alterations in circulation and stratification, in addition to possible biological feedbacks (Keeling et al., 2010; Matear et al., 2000). Comparisons of repeat hydrographic cruises in the Southern Ocean show a decrease in oxygen content of the upper ocean from the 1950s to 2010s (Aoki et al., 2005; Ito et al., 2017; Matear et al., 2000) that accounts for >25% of the observed global decrease in upper ocean oxygen content (Helm et al., 2011). While higher sea surface temperatures will result in lower solubility and therefore decreased oxygen content, observed and expected changes are primarily attributed to decreased ventilation (Helm et al., 2011). This is consistent with climate model simulations, which predict decreased ventilation due to increased density stratification (Bopp et al., 2002; Keeling & Garcia, 2002; Plattner et al., 2002). The largest predicted changes in ocean oxygen content are projected to occur south of 40°S (Matear et al., 2000).

The large number of processes that control oxygen concentrations in the ocean and the multiple sources of variability around the mean state make it difficult to disentangle long-term changes from short-term variations (Ito & Deutsch, 2010). Surface oxygen concentrations equilibrate relatively quickly with the atmosphere, staying close to the saturation concentration, with significant deviations due to temperature-induced solubility changes and photosynthetic oxygen production during the formation of organic matter. Oxygen concentrations at depth reflect the combined influences of the solubility and saturation state during water mass formation and an accumulated respiration signal as organic matter sinks below the euphotic zone and is degraded.

Air-sea oxygen fluxes are an important constraint in understanding atmospheric measurements of oxygen and carbon dioxide (Keeling et al., 1993) and uncertainty in global air-sea oxygen fluxes is a primary source of uncertainty in the partitioning of ocean and land carbon sinks from atmospheric measurements (Manning & Keeling, 2006). Surface fluxes of oxygen can also be used to calculate large-scale net community

production (Nevison et al., 2012). Previous efforts to estimate air-sea oxygen fluxes directly from surface measurements over large areas have been hindered by sparse data and significant uncertainty in the air-sea flux parameterizations (Najjar & Keeling, 2000). In contrast, model-based inversion estimates rely on correct ocean transport models and assumptions of steady state (Gruber et al., 2001).

In order to assess actual changes to ocean oxygen fluxes and concentration, it is necessary to develop a baseline of oxygen measurements covering a large spatial and temporal range to distinguish variability on seasonal, annual, interannual, and decadal time scales from a long-term trend driven by climate change and warming. With repeat hydrography cruises in the Southern Ocean many years or decades apart and biased toward the summer, and with little information on the seasonal cycle, it is difficult to know the background variability in this region. Oxygen data from autonomous profiling floats have the potential to provide the spatial and temporal coverage needed to establish current variability and determine whether previously observed trends in Southern Ocean oxygen content rise above natural spatial and temporal variability. Three recent developments have now made it possible to use these measurements to greatly improve understanding of the oxygen cycle in this region.

First, a recent recalibration of Argo oxygen data has greatly improved the quality of available Argo oxygen data in the Southern Ocean over the last decade (Drucker & Riser, 2016). Early Argo oxygen measurements suffered from substantial calibration uncertainty, making interpretation of air-sea gas exchange difficult and intercomparison problematic (Bittig & Körtzinger, 2015; D'Asaro & McNeil, 2013; Emerson & Bushinsky, 2014; Gruber et al., 2009). Postdeployment reanalysis using climatology and assumptions about saturation improved the accuracy to $\pm$1–3% (Takeshita et al., 2013), which was still too uncertain to accurately calculate air-sea exchange. The recent reanalysis of older Argo oxygen measurements using spatially matched historical cruise data has now significantly improved accuracy of the historical Argo array to several tenths of a percent, below the threshold needed for air-sea exchange calculations (Drucker & Riser, 2016).

Second, development of in situ air calibrations of one type of oxygen sensor, Aanderaa optodes, has further increased initial in situ accuracy to better than a percent in the surface ocean (Bittig & Körtzinger, 2015; Bushinsky & Emerson, 2013; Bushinsky et al., 2016; Emerson & Bushinsky, 2014; Fiedler et al., 2013; Johnson et al., 2015), making it possible to calculate air-sea fluxes and separate the physical and biological processes that affect oxygen changes. Over the past 3 years, more than 70 floats with air-calibrated oxygen sensors have been deployed in the Southern Ocean as part of the Southern Ocean Carbon and Climate Observations and Modeling (SOCCOM) project.

Finally, over the past several years, evaluations and modifications to air-sea gas flux parameterizations have further reduced uncertainty in the calculation of air-sea oxygen fluxes. Bubble injection is an important component of the air-sea gas fluxes of relatively insoluble gases such as oxygen (Liss & Merlivat, 1986). Uncertainty about bubble injection and whether to implicitly include it in a single parameterization driven by the air-sea oxygen gradient, such as the Wanninkhof (1992) parameterization developed for carbon dioxide, or in one or more explicit bubble fluxes (Liang et al., 2013; Stanley et al., 2009; Woolf & Thorpe, 1991) has long been a barrier to accurate calculation of air-sea oxygen exchange from surface oxygen measurements. Recent work evaluating a range of gas flux parameterization models with empirical data (Emerson & Bushinsky, 2016) and further refinements to the importance of the bubble flux component (Yang et al., 2017) have significantly reduced these uncertainties. While further advances will continue to lower uncertainty, these improvements to the air-sea oxygen parameterization allow analysis of the Argo oxygen data set for calculation of large-scale air-sea fluxes and add to our understanding of biological and physical processes in the ocean and how they impact the carbon cycle.

In this paper, we outline the use of the newly reanalyzed historical Argo oxygen data set and the recently deployed SOCCOM floats to improve our understanding of the Southern Ocean oxygen cycle. We combine the new Argo data with a recent gas flux parameterization to describe the seasonal cycle of oxygen saturation and fluxes in four Southern Ocean provinces, including a strong net flux of oxygen to the ocean in the seasonally ice-covered ocean. We separate the thermal oxygen flux from the total flux for each region and determine the relationship of the nonthermal flux to net primary production and mixed layer depth. These analyses allow us to describe the processes controlling both seasonal changes in the air-sea oxygen flux and the long-term balance of the total, thermal, and nonthermal fluxes.

2. Methods

2.1. Southern Ocean Regions

The Southern Ocean is divided into four distinct biogeochemical provinces though application of the Orsi et al. (1995) criteria to a 10 year Argo temperature and salinity climatology (Roemmich & Gilson, 2009) (Figure 1a). As we shall see, these provinces exhibit different seasonal patterns of oxygen supersaturation and flux. Floats are quasi-Lagrangian drifters which do not necessarily stay within a given water mass. In order to account for floats crossing regional boundaries during their deployments, each float profile is separated into one of the four provinces based on its geographic coordinates. The Subtropical Zone (STZ) extends

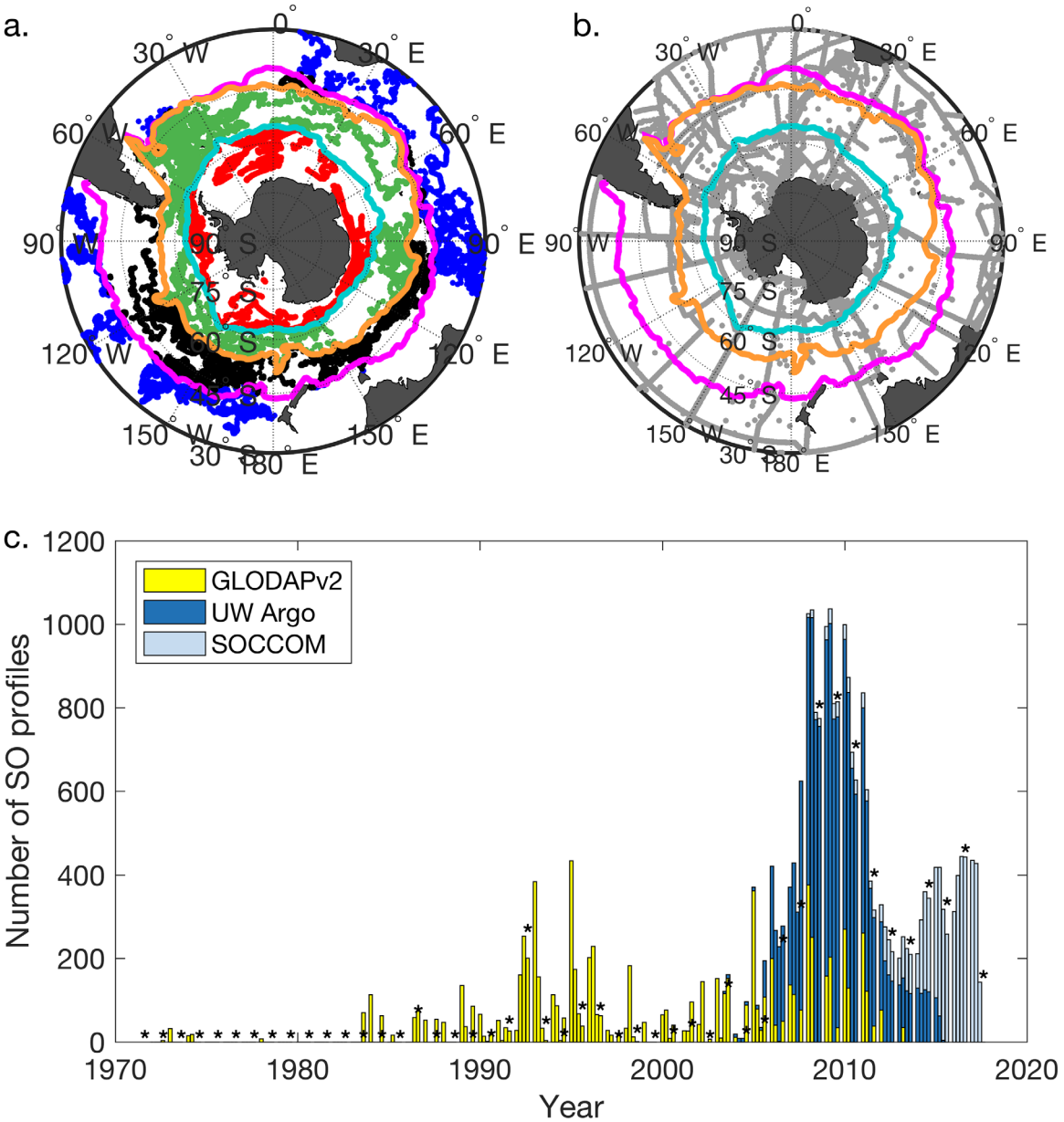

Figure 1. Float and cruise profile distribution in space and time. (a) Float profiles used for seasonal oxygen cycle and flux calculations colored by biogeochemical province: Subtropical Zone (blue points, magenta southern boundary), Subantarctic Zone (black points, orange southern boundary), Polar Frontal-Antarctic Zone (green points, teal southern boundary), and Seasonal Ice Zone (red). (b) GLODAPv2 cruise sample locations (light gray points). (c) Number of Southern Ocean profiles in each season (summer: DJF, fall: MAM, winter: JJA, and spring: SON), differentiated by GLODAPv2 cruise data (yellow), UW Argo data set (dark blue), and SOCCOM float profiles (light blue). Note that one cruise profile contains 24–36 samples, while a float profile contains ~150 to 200 measurements. Asterisks mark winter bar for each year.

from 30°S to the Subtropical Front, defined where the potential temperature (θ) at 100 dbar equals 11°C. The STZ encompasses an area of 3.93×10^{13} m^2. The average summertime (DJF) mixed layer depth (MLD, calculated from float measured temperature and salinity using de Boyer Montégut et al., 2004, 0.2°C θ threshold) is 31 ± 13 m, deepening to a max of 135 ± 83 m in the winter (JJA) (Figure 2, monthly values in Table 1). Uncertainties for temperature, nitrate, and MLD represent ± 1 pooled standard deviation, which includes both variance within each region as well as interannual variability in the mean values. Summertime production is nitrate limited (Pollard et al., 2002), with nitrate dropping to 0.5 ± 0.5 μmol kg^{-1} by mid-March before rising back to a seasonal maximum of 4.5 ± 1.6 μmol kg^{-1} in October (nitrate measured on SOCCOM Argo floats equipped with an ISUS nitrate sensor; Johnson et al., 2017a).

The Subantarctic Zone (SAZ, area $= 1.96 \times 10^{13}$ m^2) lies between the Subtropical Front and the Subantarctic Front (location where θ at 400 dbar equals 5°C) and is characterized by deep wintertime mixed layer depths, reaching a mean of 280 ± 140 m in September, before rising to 48 ± 21 m in January. Nitrate is never fully drawn down in this region, with minimum float measured values observed in January of 8.3 ± 3.1 μmol kg^{-1} and maximum values of 16 ± 3.1 μmol kg^{-1} occurring in August, during maximum exchange with deep waters. The amplitude of the seasonal nitrate change is greater in this region than in any of the others.

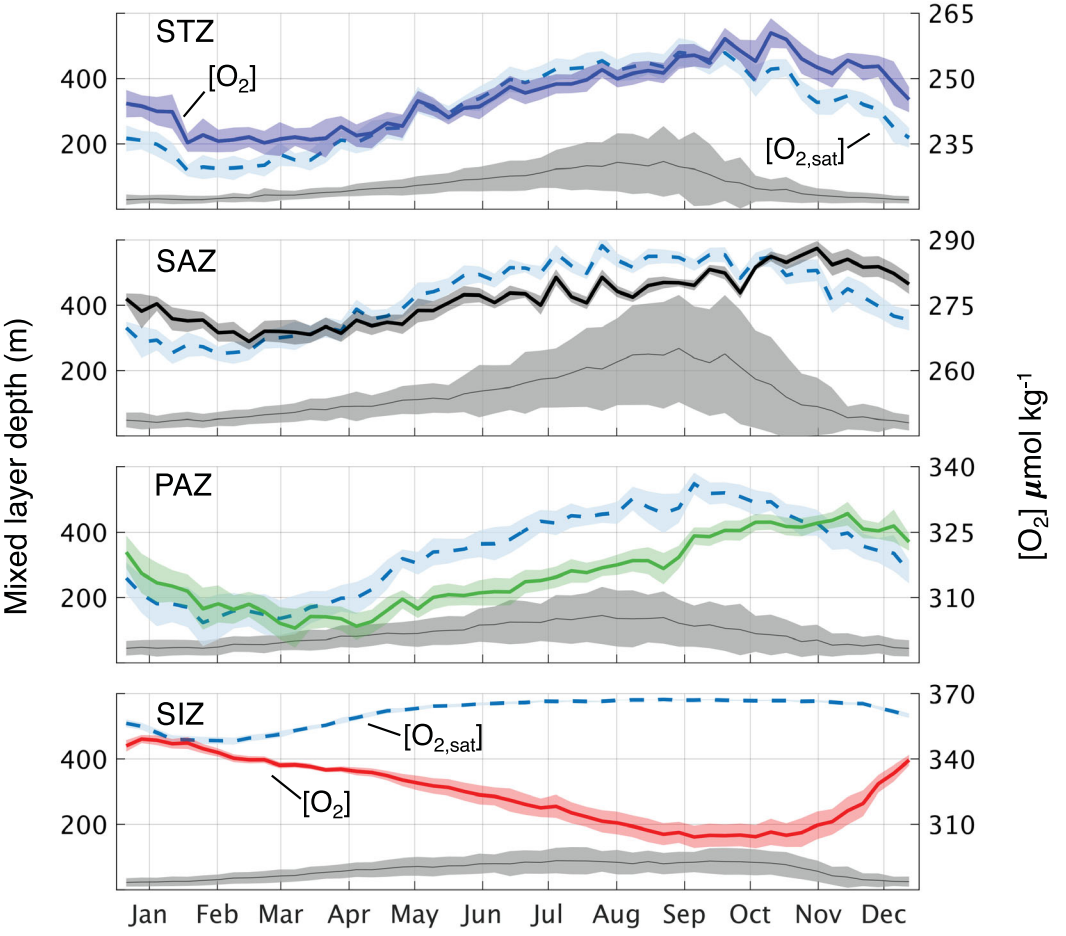

Figure 2. Regional float-derived mixed layer depths, oxygen concentration, and saturation. Float measurements from 2008 to 2016 were combined and averaged into one annual cycle for each biogeochemical province. Mixed layer depths (left axis, gray lines/areas: mean $\pm$ 1 standard deviation) were calculated using float measured temperature and salinity (de Boyer Montégut et al., 2004). Mean oxygen concentration (solid lines/colored areas, right axis) and saturation (García & Gordon, 1992; dashed blue lines/areas) are plotted with areas representing ± 1 standard error. The deepest and most variable mixed layers are in the SAZ, while the SIZ has the shallowest winter mixed layer depths and the least variability. Note that the right axis range for the STZ, SAZ, and PAZ is 45 μmol kg^{-1} and for the SIZ is 90 μmol kg^{-1}, in order to display the wide range in oxygen concentrations measured by the floats.

Table 1
Regional Characteristics

	STZ			SAZ			PAZ			SIZ		
	T (°C)	NO_3 (μmol kg^{-1})	MLD (m)	T (°C)	NO_3 (μmol kg^{-1})	MLD (m)	T (°C)	NO_3 (μmol kg^{-1})	MLD (m)	T (°C)	NO_3 (μmol kg^{-1})	MLD (m)
Jan	18.9 ± 3.3	1.7 ± 0.6	30 ± 13	11.7 ± 2.3	8.3 ± 3.1	48 ± 21	4.9 ± 2.7	22 ± 3.7	49 ± 25	−0.3 ± 0.9	28 ± 1.7	25 ± 13
Feb	19.3 ± 3	1.8 ± 0.5	32 ± 12	11.9 ± 2.2	8.9 ± 3	54 ± 20	4.8 ± 2.3	23 ± 2	56 ± 24	0.2 ± 0.9	26 ± 1.3	34 ± 17
Mar	19.1 ± 2.6	0.5 ± 0.5	47 ± 19	11.9 ± 2.2	9.4 ± 4	70 ± 26	5.3 ± 3.1	21 ± 1.4	66 ± 29	0 ± 1	28 ± 1.5	43 ± 20
Apr	18.6 ± 2.6	1.6 ± 0.3	56 ± 16	11.2 ± 2	9.8 ± 3.2	90 ± 36	4.9 ± 3.1	21 ± 1.9	81 ± 32	−0.8 ± 1	29 ± 1.5	59 ± 21
May	17.2 ± 2.7	2.5 ± 1.4	69 ± 26	10 ± 2	12 ± 3.1	120 ± 39	4.1 ± 2.9	20 ± 1.9	95 ± 38	−1.4 ± 0.7	30 ± 1.1	70 ± 26
Jun	16.2 ± 2.5	0.7 ± 0.4	93 ± 35	9.1 ± 1.9	13 ± 3.1	140 ± 53	3.8 ± 3.1	20 ± 2.5	120 ± 50	−1.6 ± 0.6	29 ± 1.3	79 ± 29
Jul	14.9 ± 2.3	1.8 ± 1.1	120 ± 45	8.6 ± 1.8	14 ± 2.9	190 ± 76	3.1 ± 2.9	21 ± 2.9	130 ± 65	−1.7 ± 0.4	30 ± 1	84 ± 29
Aug	14.5 ± 2.4	2.7 ± 1.3	140 ± 67	8.5 ± 1.5	16 ± 3.1	270 ± 120	2.5 ± 2.7	23 ± 2.2	140 ± 71	−1.8 ± 0.3	30 ± 1.3	86 ± 33
Sep	14.4 ± 2.7	3 ± 1.4	120 ± 82	8.6 ± 1.5	15 ± 3.3	280 ± 140	2.3 ± 2.9	25 ± 2.1	120 ± 59	−1.7 ± 0.3	32 ± 0.4	79 ± 34
Oct	14.5 ± 2.6	4.5 ± 1.6	68 ± 55	8.7 ± 1.6	15 ± 3.6	210 ± 170	2.2 ± 2.7	24 ± 2.1	93 ± 57	−1.7 ± 0.3	32 ± 0.8	75 ± 30
Nov	15.8 ± 3	3 ± 1.3	43 ± 26	9.4 ± 1.9	13 ± 4	91 ± 90	3.1 ± 3.1	22 ± 2.7	66 ± 41	−1.6 ± 0.4	30 ± 1.1	46 ± 27
Dec	17.1 ± 3.1	1.6 ± 1.2	31 ± 12	10.4 ± 2.7	11 ± 3.3	54 ± 38	3.9 ± 2.9	23 ± 3.5	49 ± 27	−1.2 ± 0.7	29 ± 1.8	26 ± 15

Note. Mean and standard deviation of temperature, nitrate, and mixed layer depth for all regions from 2008 to 2016. Uncertainty (±1 standard deviation) includes both spatial and temporal variability. Nitrate was measured only on SOCCOM Argo floats equipped with an ISUS nitrate sensor (see Johnson et al., 2017a, for calibration and accuracy information). Mixed layer depths were calculated from float measured temperature and salinity (de Boyer Montégut et al., 2004).

The Polar Frontal-Antarctic Zone (PAZ, area = 2.69 × 10^{13} m^2) extends from the Subantarctic Front to the September extent of sea ice (15% concentration) for the 2014–2015 winter. Mean winter MLDs in the PAZ are 130 ± 69 m, similar to the STZ, while summertime MLDs average 48 ± 26 m. The seasonal nitrate drawdown is ~4 to 5 μmol kg^{-1}, with minimum values measured from March to June, and a maximum in September.

The Seasonal Ice Zone (SIZ, area = 1.73 × 10^{13} m^2) consists of waters seasonally capped by sea ice which reduces the light available for photosynthesis and limits air-sea gas exchange. The SIZ displays the shallowest wintertime mixed layers of the four regions, with a winter mean of 82 ± 35 m and a summer mean of 27 ± 16 m. The seasonal amplitude of nitrate drawdown is similar to the PAZ, though the observed magnitude of mixed layer nitrate is greater, with a low in February of 26 ± 1.3 μmol kg^{-1} and a high in September of 32 ± 0.4 μmol kg^{-1}. The seasonal temperature change is smallest in the SIZ, from a winter low of −1.8 ± 0.3°C in August to a maximum of 0.2 ± 0.9°C in February. While under ice, floats are unable to determine their position using GPS. Latitude and longitude for under ice profiles are determined using a linear interpolation between their last fall and first spring positions.

2.2. Float Oxygen Measurements

The float oxygen data used in this study are a mix from two sources. Quality controlled oxygen data downloaded from the SOCCOMviz data portal (63 floats, http://soccom.princeton.edu/soccomviz.php; Johnson et al., 2017b) are primarily from air-calibrated Aanderaa optodes mounted on APEX floats deployed as part of the SOCCOM program. A subset (15 floats) of the SOCCOMviz floats are either Sea-Bird 63 optodes on Navis floats or older APEX floats; these float types lack air-calibration capability and were calibrated against deployment cruise data. The air-calibrated optodes make at least one atmospheric oxygen measurement after each profile, yielding an in situ calibration reference. The partial pressure of oxygen in the atmosphere can be calculated from total atmospheric pressure, the mole fraction of oxygen, and water vapor pressure. Atmospheric pressure was interpolated in time and space from the National Centers for Environmental Prediction (NCEP) reanalysis product. The mean offset from expected atmospheric pO_2 is used to calculate a multiplicative gain correction to adjust the entire data set (Johnson et al., 2015, 2017a). Calibrations were performed by SOCCOM with detailed calibration information presented in Johnson et al. (2017a).

The second source of float data is the University of Washington (UW) Argo oxygen reanalysis from Drucker and Riser (2016), (v1.1), which consists of UW Argo oxygen floats deployed from July 2003 to December 2013 that have been corrected to historical cruise data and a seasonal cycle of oxygen at the surface,

yielding two point calibrations for each float. If floats were present in both data sets, the SOCCOMviz data were used, leaving 87 floats in the UW Argo oxygen data set. The 150 floats used in this study completed a total of 19,768 profiles from 2003 to 2016 (Figure 1c). Surface records of oxygen, temperature, and salinity were visually assessed and profiles with large, transient excursions in only one parameter, indicative of sensor error rather than a change in ocean properties, were removed from the record (approx. 21 profiles).

Only data from 2008 to 2016 are used in the seasonal cycle and flux analyses. In order to test for spatial biases in the combined float oxygen record, monthly mean temperature for each region was compared to the matching mean temperature calculated from the daily NOAA Optimal Interpolation Sea Surface Temperature data set (NOAA OI SST, supporting information, Figure S1). Months where the standard deviation of each data set did not overlap with the mean of the other data set were filtered from later analyses (26 months removed from the STZ out of 108 total, 7 out of 108 from the SAZ, 8 out of 108 from the PAZ, and 26 out of 108 from the SIZ).

2.3. Comparison to Shipboard Data

To check the UW Argo data set for biases or offsets, cruise data were retrieved from the Global Ocean Data Analysis Project Version 2 (GLODAPv2) database (Key et al., 2015; Olsen et al., 2016). The GLODAP program filters and adjusts data to be consistent across cruise line intersections and bad data are flagged and removed. Only data flagged "good" were used for this analysis. Data from 8,415 profiles south of 30°S on 132 cruises (Figures 1b and 1c) were used for comparison with UW Argo data (Figure 3). The SOCCOM oxygen data set was evaluated against deployment cruises during the SOCCOM period. High oxygen gradients and the relatively slow response time of the Aanderaa optode sensors make it difficult to effectively compare float oxygen measurements to bottle-sampled Winkler measurements in the thermocline and at the base of the mixed layer. In order to avoid data mismatches in this section of the water column, measurements from 200 m below the base of the mixed layer to 5 m above were removed from this analysis.

2.4. Air-Sea Flux Calculations

Parameterizations for estimation of air-sea fluxes as a function of wind speed are in on-going development. In particular, the contribution of bubble injection to the total flux for relatively insoluble gases such as oxygen has been identified as an important component of the total flux. A recent assessment of air-sea flux parameterizations (Emerson & Bushinsky, 2016) against in situ noble gas ratios and mooring measurements identified the Woolf (1997) and Liang et al. (2013) formulations as best able to reproduce observations. The Liang et al. (2013) model used here models both large and small bubbles, better explaining measurements of relatively insoluble gases such as oxygen than models without bubbles (Emerson & Bushinsky, 2016). The bubble contribution of Liang et al. (2013) was further tuned in Yang et al. (2017) to in situ mooring

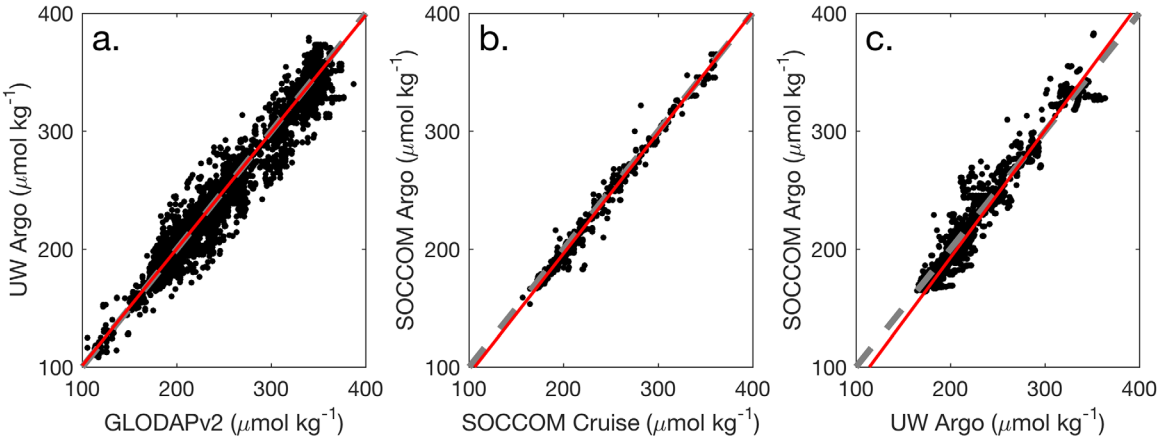

Figure 3. Float and cruise oxygen comparisons. Individual data set comparisons were made between (a) UW Argo and GLODAPv2 cruise data and (b) SOCCOM Argo and SOCCOM deployment cruise data to verify data sets using the closest cruise data in time. Cruise and float data were matched to within ±5–10 days from any year, ±10 db pressure, and ±0.25°–0.5° latitude (details in Table 2). UW Argo and SOCCOM float measurements were compared by finding matches within ±5 days from any year, 0.25° latitude, and ±10 db pressure. Data in the high oxygen gradient region at the base of the mixed layer and in the thermocline were removed by removing matchups from 5 m above the base of the mixed layer to 200 m below. Model II regressions (red lines) between data comparison were used to evaluate differences across the range of surface oxygen concentrations (regression statistics and results in Table 2). Dashed lines are 1:1.

measurements of N_2 gas using the upper ocean mixed layer model of Bushinsky and Emerson (2015) to adjust the bubble contribution to the total flux:

$$F_{A-W} = F_s + \beta F_c + \beta F_p \quad (1)$$

where F_{A-W} is the total air-water gas flux (positive to the atmosphere), F_s is the diffusive component, F_c is the flux component due to small bubbles that completely collapse, F_p is the component due to large bubbles that partially collapse before returning to the ocean surface, and β (0.29) is the tuning parameter used to produce the best fit between the flux parameterization and the mooring observations. Liang et al. (2013) calculates F_s as:

$$F_S = 1.3\times10^{-4} U_a^* \left(\frac{S_{O_2}}{660}\right)^{-0.5} \left([O_2] - [O_{2,sat}]\right) \frac{\rho_w}{10^6} \quad (2)$$

from the NOAA-COAREG algorithm (Fairall et al., 2011) that explicitly separates the diffusive and bubble components of air-sea exchange. U_a^* is the air-side friction velocity, a function of the drag coefficient and wind speed, S_{O_2} is the Schmidt number, $[O_{2,sat}]$ is the oxygen saturation concentration calculated from García and Gordon (1992), and ρ_w is the seawater density. The small, completely collapsing bubble component is calculated as:

$$F_C = -5.56 \left(U_w^*\right)^{3.86} X_{O_2} \quad (3)$$

where U_w^* is the water side friction velocity, which is primarily a function of wind speed and a drag coefficient, scaled by the density differences between air and water, and X_{O_2} is the mole fraction of oxygen in the atmosphere. The large, partially collapsing bubble component is:

$$F_P = 5.5 \left(U_w^*\right)^{2.76} \left(\frac{S_{O_2}}{660}\right)^{-2/3} \left([1+\Delta_P][O_2] \frac{\rho_w}{10^6} - [O_{2,sat}] \frac{\rho_w}{10^6}\right) \quad (4)$$

where Δ_p is the increase in saturation concentration within bubbles as they are driven deeper in the ocean at higher wind speeds.

Wind speeds were spatially interpolated from the Cross-Calibrated Multi-Platform (CCMP) daily gridded wind product through May 2016 (http://www.remss.com/measurements/ccmp) and the European Centre for Medium-Range Weather Forecasts ERA-Interim (Dee et al., 2011; http://apps.ecmwf.int/datasets/data/interim-full-daily/levtype=sfc/) daily wind speed product for June 2016 to December 2016 when CCMP output was unavailable. An overlap period between the two wind products was assessed and no significant difference was found in wind speed or distribution. Due to the nonlinearity of air-sea gas exchange as a function of wind speed, it is necessary to calculate air-sea fluxes using the same temporal resolution as the wind speeds used in the air-sea flux parameterization. Float measurements were interpolated to a daily record used to match the air-sea flux parameterizations for oxygen. For under ice floats, air-sea fluxes were scaled linearly (McNeil et al., 2007) according to sea-ice cover:

$$F_{total} = F_{A-W}(1-\gamma) \quad (5)$$

where γ is the sea-ice fraction derived from Nimbus-7 SMMR and DMSP daily product (Cavalieri et al., 1996) for data prior to 31 December 2015 and the Near-Real-Time DMSP daily gridded sea ice concentrations (Maslanik & Stroeve, 1999) for 1 January 2016 onward.

2.5. Air-Sea Flux Uncertainties

Oxygen concentration uncertainty was set to ±1.5% based on the comparison to shipboard measurements and data set intercomparison presented in section 3.1. In situ drift has been demonstrated in float mounted optodes (Bittig & Körtzinger, 2017; Bushinsky et al., 2016; Drucker & Riser, 2016) on the order of a few tenths of a percent per year. Optodes in the UW Argo data set are corrected according to matchups throughout their lifetime, so drift should be eliminated in the reanalyzed Drucker and Riser (2016) data set. Any drift in the SOCCOM-deployed floats should fall within the ±1.5% uncertainty used in this uncertainty analysis.

Atmospheric pressure from NCEP was given an uncertainty of 0.1% (~1 mbar), which directly influences the atmospheric values of pO_2. One advantage of air-calibrated oxygen is that if the same pressure estimate is

used for air calibration and air-sea flux estimates, any uncertainty in the atmospheric pressure cancels out in a final error estimate (Bushinsky & Emerson, 2015).

A 20% uncertainty in the total air-sea flux calculations was used for the Liang et al. (2013) parameterization. Total uncertainty for the air-sea oxygen fluxes was calculated using a 1,500 iteration Monte Carlo estimation. Monthly mean fluxes are calculated from the individual daily float estimates for each region. Annual means are calculated from the monthly means for each year with greater than 8 months of available data. Regional means are calculated from the annual means and reported with ± 1 standard error of the mean value. These uncertainty values represent confidence in the mean flux for each region, but do not include the spatial variability within each region. With a constant variance and more years of data the standard error will decrease as confidence in the mean state increases.

Despite the large number of float profiles used in this study, it is still possible that we may be undersampling the spatial variability in these regions, potentially biasing the mean values. The evaluation of mean temperatures for each region against NOAA OI SST is one check that we have adequately sampled the spatial variability within each region. However, while a reconstruction of the regional temperature can give an idea of how well thermally driven fluxes are sampled by the Argo floats, this does not account for the potentially greater variability in the oxygen fluxes due to biological processes. One way to assess the impact of float sampling location relative to the total spatial variability in the Southern Ocean is to subsample high-resolution ocean models. CM2.6 is a coupled climate model with a 0.1° resolution ocean, run with a simple biogeochemical model (Delworth et al., 2012; Galbraith et al., 2010, 2015). Subsampling the model daily fluxes at the float locations and times and comparing those results to the full monthly means for those regions gives one realization of potential biases in the float-based results due to undersampling of spatial variability (supporting information Figure S2 and Table S1). These results are discussed in section 3.2.

3. Results and Discussion

3.1. Combined Data Set Accuracy

The UW Argo oxygen data set and the SOCCOM air corrected floats use calibration methods that differ in how the correction is determined and applied. While both of these methods have been independently validated (Drucker & Riser, 2016; Johnson et al., 2017a), in order to merge these data sets to analyze the entire Argo oxygen record in the Southern Ocean it is necessary to assess them for systematic differences. The UW Argo and SOCCOM air-calibrated float samples were compared to each other and bottle Winkler measurements collocated in space and time of year (Figure 3) from the GLODAPv2 data set (UW Argo) and the SOCCOM deployment cruises (SOCCOM data). Crossovers were matched in time by day of the year, from any year of the data set in order to have sufficient points for analysis. Model II linear regressions were calculated for each data comparison and data set differences were calculated at 325 and 250 μmol kg^{-1}, which represents the range of the majority of the surface data used in this analysis (Table 2).

UW Argo float measurements were paired with GLODAPv2 measurements within ± 10 days (in any year), 0.5° latitude, and 10 db (Figure 3a). At 325 μmol kg^{-1}, the regression between UW Argo oxygen data and GLODAPv2 gives a -0.9 μmol kg^{-1} difference between the concentration expected based on the GLODAPv2 data and the equivalent float concentration, while at 250 μmol kg^{-1} the difference is -0.2 μmol

Table 2
Oxygen Data Set Comparison

	Comparison criteria				Model II regression statistics			Offset at (μmol kg^{-1}):	
Data sets compared	Dist (° lat.)	Days	Press. (db)	n	Slope	Intercept	r	325	250
UW Argo versus GLODAPv2	±0.5	±10	±10	9,771	0.99	2.2	0.98	−0.9	−0.2
SOCCOM Argo versus Deployment Cruises	±0.25	±5	±10	614	1.02	−8.5	0.99	−0.8	−2.6
UW Argo versus SOCCOM Argo	±0.25	±5	±5	4,997	1.08	−23.5	0.97	2.7	−3.3

Note. Data set comparison criteria and statistics for model II regression. In addition to the criteria above, all matched points were filtered to remove points from 5 m above to 200 m below the mixed layer depth to avoid data mismatches in the high oxygen gradient region of the water column.

kg^{-1}. SOCCOM float oxygen within ±5 days (in any year), 0.25° latitude, and 10 db pressure were plotted against SOCCOM deployment cruise oxygen measurements (Figure 3b) yielding an offset at 325 μmol kg^{-1} of −0.8 μmol kg^{-1} and at 250 of −2.6 μmol kg^{-1}.

UW Argo data were compared with SOCCOM Argo data that overlapped within ±5 days, 0.25° (27.8 km), and 5 db (Figure 3c). The difference at 325 μmol kg^{-1} is 2.7 μmol kg^{-1} (∼0.8%), and at 250 μmol kg^{-1} is −3.3 μmol kg^{-1} (∼1.3%). To account for these apparent differences, a conservative ±1.5% uncertainty was used in all oxygen flux calculations.

The accuracy of this combined data set is better than 1.5%, which allows for assessment of the air-sea oxygen flux. It is unclear whether the offsets between the data sets are due to water mass mismatches, individual sensor inaccuracies, or systematic biases. The comparison between UW Argo and SOCCOM Argo assumes no significant change in Southern Ocean oxygen concentrations during the ∼10 years of measurements. The SOCCOM Argo oxygen measurements at lower oxygen concentrations appear to be low of both the deployment cruises and the UW Argo oxygen data set. This is consistent with prior work indicating that a gain correction of the surface values using atmospheric calibration does not fully correct for the low-oxygen bias due to drift at deep measurements with higher pressures, lower temperatures, and lower oxygen concentrations (Bushinsky et al., 2016; Drucker & Riser, 2016). The reason for a different drift at deeper, lower oxygen measurements is not currently clear. As such, rather than correct for this potential bias, we use an uncertainty that encompasses the difference at lower oxygen concentrations. Atmospheric calibration of oxygen sensors offers the potential to deliver higher-accuracy measurements, but is only just being utilized in large numbers configured for optimal calibration. Future validation of Argo oxygen measurements to a few tenths of a percent must be resolved in order to use the Argo oxygen array to assess previously reported oxygen changes on the order of tenths of μmol kg^{-1} yr^{-1} in deeper ocean waters.

3.2. Air-Sea Oxygen Gradient and Annual Flux

The difference in concentration from saturation ($\Delta[O_2] = [O_2] - [O_2]_{sat}$, Figure 4 and Table 3) drives air-sea gas exchange. In the STZ, the seasonal amplitude of $\Delta[O_2]$ is ∼12 μmol kg^{-1} with slightly undersaturated waters in the winter and a maximum early summer $\Delta[O_2]$ peak of 8.8 ± 2.3 μmol kg^{-1} in December (uncertainties for monthly, seasonal, and annual $\Delta[O_2]$ and oxygen fluxes represent ±1 standard error of the mean). The peak $\Delta[O_2]$ in the SAZ also occurs in December with a value of 7.8 ± 3.3 μmol kg^{-1} and 1 month later in the PAZ with a $\Delta[O_2]$ in January of 6 ± 2.5 μmol kg^{-1}. Larger wintertime oxygen deficits in these two regions result in a $\Delta[O_2]$ amplitude of ∼15 μmol kg^{-1} in the SAZ and ∼19 μmol kg^{-1} in the PAZ. The SIZ, with seasonal exposure of deep upwelled waters significantly undersaturated in oxygen but restricted from quickly equilibrating with atmospheric oxygen by sea ice, exhibits the greatest seasonal amplitude of ∼52 μmol kg^{-1}, driven mainly by a strong deficit in $\Delta[O_2]$, reaching a minimum of −57 ± 11 μmol kg^{-1} by September, 1–2 months later than the more northern provinces. The annual average $\Delta[O_2]$ of the STZ is 3 ± 1.6 μmol kg^{-1}, while mean $\Delta[O_2]$ in the SAZ is near zero (0.1 ± 1.3 μmol kg^{-1}), in the PAZ is −5 ± 3 μmol kg^{-1} and in the SIZ is −28 ± 4 μmol kg^{-1} (Figure 4).

The seasonal cycle of temperature and biology combine to reinforce a seasonal gas exchange cycle, with warm waters during the summer decreasing the solubility of the water and coinciding with the biological production of oxygen, both of which increase oxygen supersaturation and outgassing. The seasonal cycle of air-sea oxygen fluxes varies in timing and magnitude between the four regions, closely following seasonal cycles of $\Delta[O_2]$ but biased toward larger absolute fluxes in the wintertime when high wind speeds inject oxygen into the ocean (Table 4). The STZ outgasses oxygen on an annual basis, with an efflux of 1.2 ± 0.7 mol O_2 m^{-2} yr^{-1} (Figure 5, positive fluxes to the atmosphere), largely driven by a large summertime outgassing flux. Annual fluxes decrease to the south. The SAZ has an annual flux of −1.3 ± 0.6 mol O_2 m^{-2} yr^{-1}, with roughly balanced summer and winter fluxes and smaller fluxes in the fall and spring. The PAZ is a net sink of −3.5 ± 1.1 mol O_2 m^{-2} yr^{-1}. A strong summertime outgassing in the PAZ is outweighed by moderate influxes during the fall and spring and a strong influx in the winter. The SIZ has very weak summertime outgassing and a consistent strong influx of oxygen from fall to spring that drives a mean annual flux of −6.4 ± 0.5 mol O_2 m^{-2} yr^{-1}.

The total annual oxygen flux in the Southern Ocean (south of 30°S) is −183 ± 80 Tmol O_2 yr^{-1} (Table 5), comprised of an outgassing in the STZ of 47 ± 29 Tmol O_2 yr^{-1}, and influxes in the SAZ of −25 ± 12 Tmol O_2 yr^{-1}, in the PAZ of −94 ± 30 Tmol O_2 yr^{-1}, and in the SIZ of −111 ± 9.3 Tmol O_2 yr^{-1}. Previous

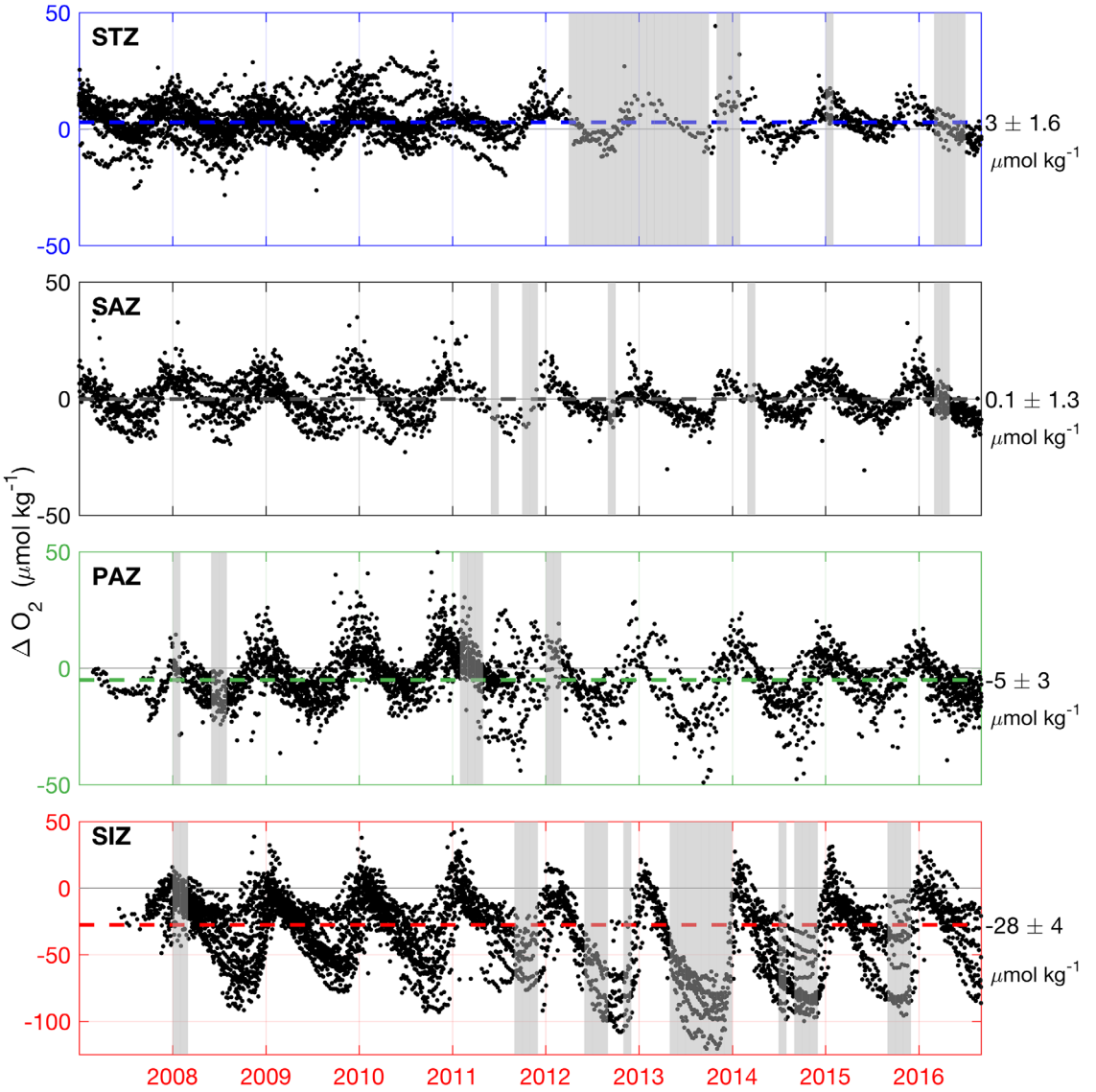

Figure 4. $\Delta[O_2]$ ($\Delta[O_2] = [O_2]_{measured} - [O_2]_{saturation}$) calculated from the near-surface values for each float profile split by regional definitions. Gray bands indicate months where mean float SST did not match NOAA OISST data (supporting information Figure S1) and which were removed from all analyses. Mean annual $\Delta[O_2]$ (2008 through the end of 2016, ± 1 SE) for each region is labeled to the right of each region (dashed lines indicate the mean on each plot). In the STZ, SAZ, and PAZ, the peak $\Delta[O_2]$ is in December, with a minimum in July. The SIZ exhibits the largest seasonal cycle, with a minimum $\Delta[O_2]$ in September of -57 ± 11 μmol kg^{-1} undersaturation. Note the extended *y* axis limit for the SIZ.

estimates of oxygen air-sea fluxes over ocean basins were possible only from climatological means (Garcia & Keeling, 2001; Najjar & Keeling, 2000) or inversion models based on interior oxygen concentrations and an ocean transport model (Gruber et al., 2001). We compare our total oxygen fluxes to the data inversion estimate of Gruber et al. (2001) because it is independent of air-sea flux parameterizations and has the Southern Ocean divided into useful regions of comparison.

Gruber et al. (2001) present two air-sea oxygen flux estimates using the same ocean model and interior oxygen measurements: one constrained to a net global air-sea oxygen flux of zero and an unconstrained version. We will primarily compare our results with their constrained model (Figure 6). In the Southern Ocean region south of 36°S, we calculate a flux of -221 ± 57 Tmol O_2 yr^{-1}, twice the oceanic uptake in Gruber et al. (2001) of -108.2 Tmol O_2 yr^{-1}. This area is further divided into three subregions: the Subpolar South Pacific and Subpolar South Indian Ocean (hereafter Subpolar South Indo-Pacific), the Subpolar South Atlantic, and an area south of 58°S. In the Subpolar South Indo-Pacific region, we calculate an influx of

Table 3
Δ [O_2]

μmol kg^{-1}	STZ	SAZ	PAZ	SIZ
Summer	7.2 ± 1.2	6.8 ± 1.2	4.3 ± 1.7	−13 ± 3.9
Dec	8.8 ± 2.3	7.8 ± 3.3	5.5 ± 2.9	−29 ± 9.5
Jan	6.8 ± 2.3	7.7 ± 2	6 ± 2.5	−5 ± 6.8
Feb	6.2 ± 1.9	5 ± 1.9	1.1 ± 3.3	−4.9 ± 4.3
Fall	2.7 ± 1.3	−1.1 ± 0.9	−5.8 ± 1.3	−23 ± 2.2
Mar	5 ± 2.5	1.6 ± 1.9	−1.4 ± 2.6	−14 ± 3.5
Apr	2.1 ± 2.2	−1 ± 1.8	−5.8 ± 2.3	−24 ± 3.6
May	0.6 ± 2.3	−3.4 ± 1.5	−9.7 ± 2.3	−31 ± 4.7
Winter	−1.9 ± 1.3	−6.2 ± 0.9	−12 ± 1.6	−42 ± 4
Jun	−1.3 ± 2.6	−4.8 ± 1.9	−11 ± 2.5	−36 ± 6.1
Jul	−2.8 ± 2.4	−6.5 ± 1.8	−13 ± 3.1	−39 ± 7.3
Aug	−1.5 ± 2.2	−7.1 ± 1.6	−13 ± 3.4	−50 ± 7.6
Spring	4.4 ± 1.3	0.1 ± 1.2	−5.4 ± 2.1	−52 ± 6.9
Sep	0.7 ± 2.3	−4.9 ± 1.8	−11 ± 4.1	−57 ± 11
Oct	5.3 ± 3.2	−0.9 ± 2.4	−6.1 ± 3.6	−56 ± 11
Nov	7.2 ± 2.3	5.9 ± 2.6	1.3 ± 3.5	−42 ± 14
Annual avg. Δ[O_2]	3 ± 1.6	0.1 ± 1.3	−5 ± 3	−28 ± 4

Note. Seasonal and monthly means and standard errors of regional Δ[O_2] ([O_2] − [O_2,sat]). Positive Δ[O_2] indicates that the ocean is supersaturated and will tend to outgas to the atmosphere. Summertime positive Δ[O_2] is a combination of biological production of oxygen and warming, which decreases the solubility of the surface waters. Winter negative Δ[O_2] is the result of biological respiration, entrainment of deep water low in oxygen due to the respiration of sinking organic matter, and the cooling effect on solubility.

Table 4
Province Fluxes

mmol O_2 m^{-2} d^{-1}	STZ	SAZ	PAZ	SIZ
Summer	19 ± 1.7	26 ± 2.2	24 ± 2.1	1.4 ± 2.5
Dec	25 ± 3.7	32 ± 3.1	27 ± 3.2	−12 ± 3
Jan	18 ± 2.7	30 ± 3.6	29 ± 1.4	7.9 ± 2.3
Feb	16 ± 1.9	16 ± 2.7	17 ± 4.3	8.1 ± 2.8
Fall	3.6 ± 2.1	−8 ± 2.2	−13 ± 3	−25 ± 2.6
Mar	11 ± 2.8	4.2 ± 2.8	3.6 ± 3.1	−13 ± 2
Apr	3.1 ± 2.4	−9.1 ± 2.5	−15 ± 2.9	−33 ± 4
May	−4 ± 3.4	−17 ± 2.2	−26 ± 2.6	−30 ± 3.8
Winter	−16 ± 2.1	−30 ± 1.8	−40 ± 3.5	−24 ± 1.4
Jun	−14 ± 4.4	−24 ± 2.1	−38 ± 6.5	−23 ± 2.5
Jul	−20 ± 3.6	−31 ± 2.7	−43 ± 7.2	−23 ± 1.4
Aug	−15 ± 3	−33 ± 3.8	−38 ± 5.2	−27 ± 2.8
Spring	6.9 ± 2.9	−3.2 ± 4.2	−10 ± 4.6	−22 ± 1.6
Sep	−6.9 ± 3.4	−25 ± 3.5	−32 ± 6.4	−24 ± 3.2
Oct	9.7 ± 3.4	−5.1 ± 2.9	−11 ± 5.7	−24 ± 1.1
Nov	17 ± 3.7	21 ± 2.4	12 ± 3.4	−17 ± 2.1
Mean annual (mol O_2 m^{-2} yr^{-1})	1.2 ± 0.7	−1.3 ± 0.6	−3.5 ± 1.1	−6.4 ± 0.5

Note. Seasonal, monthly, and annual oxygen fluxes for the four Southern Ocean regions (positive to the atmosphere). Net outgassing is found in the STZ. The SAZ, PAZ, and SIZ all are regions of net oxygen uptake, with the strength of the uptake increasing to the south. All regions display mean outgassing in the summer, when NPP is highest and mixed layers are shallowest. Conversely, the wintertime flux of oxygen is in to the ocean in all regions during the winter. Uncertainty represents ±1 standard error of the mean value over the 9 years of the data set.

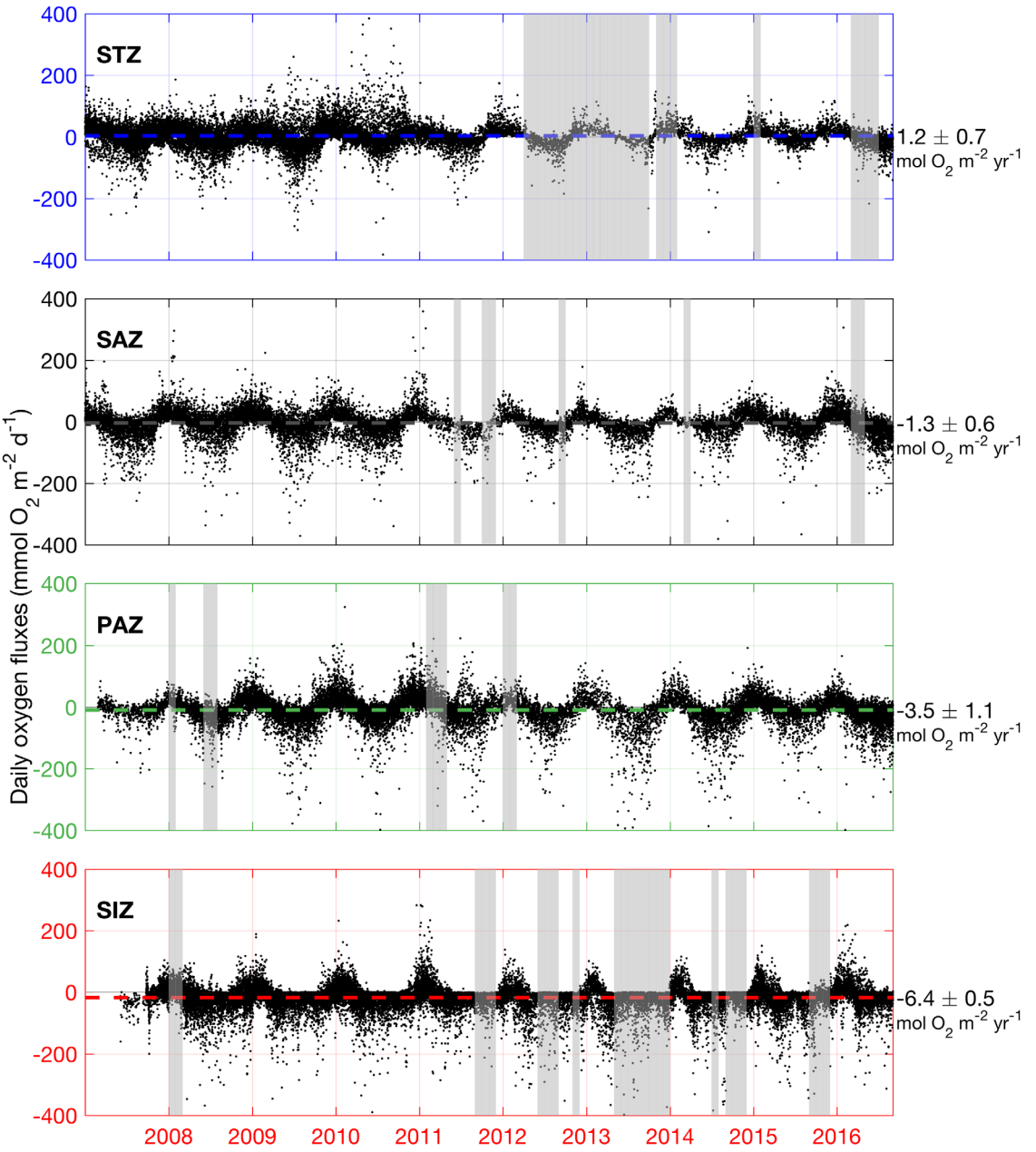

Figure 5. Air-sea oxygen flux for each region. Fluxes are calculated from daily interpolated oxygen concentrations (positive is a flux to the atmosphere). Gray bands indicate months where mean float SST did not match NOAA OI SST data (supporting information Figure S1) and which were removed from all analyses. Mean annual fluxes are to the right of each plot, with the corresponding daily flux value marked by the dashed line. Peak outgassing for each region is in December or January. In the STZ and SAZ, the maximum influx to the ocean occurs in July and in August for the PAZ. The SIZ has a relatively consistent maximum influx to the ocean from April to September.

-39 ± 38 Tmol O_2 yr^{-1}, ~36 Tmol O_2 yr^{-1} less than the Gruber et al. (2001) calculation of -74.5 Tmol O_2 yr^{-1}. This difference is roughly offset by the difference south of 58°S, where we calculate an influx of -167 ± 19 Tmol O_2 yr^{-1}, ~30 Tmol O_2 yr^{-1} greater than the Gruber et al. (2001) estimate of -136.8 Tmol O_2 yr^{-1} (section 3.4 will go into more detail on the flux south of 58°S).

The main source of the difference between this study and the Gruber et al. (2001) estimate is in the Subpolar South Atlantic, where we calculate an influx of -20 ± 8.2 Tmol O_2 yr^{-1} to their outgassing of 103.1 Tmol O_2 yr^{-1}. This region is significantly smaller than the Subpolar South Indo-Pacific oceans or the region South of 58°S, and the large flux in Gruber et al. (2001) is due to an annual oxygen outgassing of

Table 5
Total Annual Southern Ocean Fluxes

Province	Area (10^{13} m^2)	Annual fluxes (Tmol O_2 yr^{-1}) Total	Thermal	Nonthermal
STZ	3.93	47 ± 29	−2.7 ± 13	50 ± 42
SAZ	1.956	−25 ± 12	4.2 ± 5.4	−29 ± 17
PAZ	2.691	−94 ± 30	39 ± 8.2	−133 ± 38
SIZ	1.734	−111 ± 9.3	2.2 ± 2.9	−113 ± 12.2
South of 30°S	10.311	−183 ± 80	42 ± 29	−225 ± 109
Comparisons with Gruber et al. (2001) (balance constraint)				
Subpolar South Atlantic				
This study	1.563	−20 ± 8.2	22 ± 2.6	−41 ± 11
Gruber et al. (2001)	1.563	103.1	30.5	72.6
Subpolar South Pacific and Subpolar South Indian				
This study	5.027	−39 ± 38	19.4 ± 5	−58 ± 43
Gruber et al. (2001)	5.027	−74.5	−9.2	−65.2
South of 58°S				
This study	2.588	−167 ± 19	2.9 ± 2.3	−169 ± 22
Gruber et al. (2001)	2.588	−136.8	−44.1	−92.7
South of 36°S				
This study	9.178	−221 ± 57	51 ± 11	−271 ± 68
Gruber et al. (2001)	9.178	−108.2	−22.8	−85.3

Note. Total annual oxygen fluxes for the four provinces used in this study are calculated from the flux rates in Table 4 and the ocean areas listed. The thermal and nonthermal fluxes are calculated according to equations (6) and (7). For comparison, total annual fluxes were also calculated over the same regions identified in Gruber et al. (2001), with the same areas used for total flux calculation. The Subpolar South Atlantic region is from 36°S–58°S and 70°W–20°E. The Subpolar South Pacific and Subpolar South Indian region is from 36°S–58°S and 20°E–70°W. The South of 36°S and South of 58°S regions include all fluxes poleward of those latitudes.

~5.2 mol m^{-2} yr^{-1}. This outgassing flux is larger in moles per square meter than any other region in their study and counter to the general pattern of oxygen outgassing in equatorial regions and uptake at the poles. Gruber et al. (2001) attributes this outsize flux to either large-scale thermohaline circulation of waters northward in the Atlantic to replenish North Atlantic Deep Water formation or to higher biological activity in the South Atlantic.

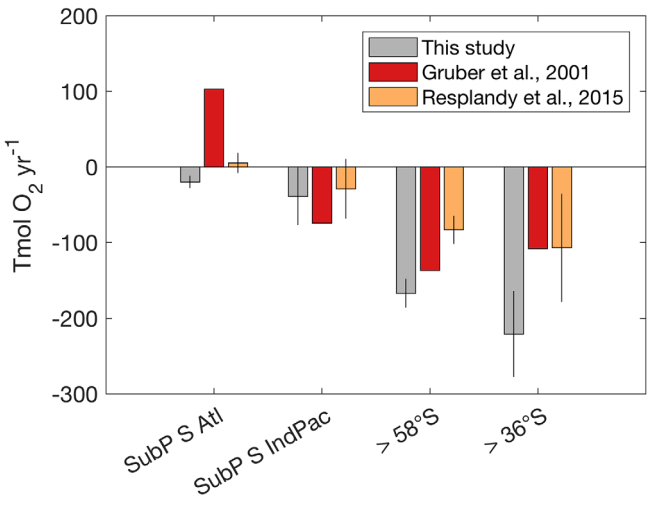

Figure 6. Summary of total oxygen flux comparisons presented in the text and in Table 5. Gruber et al. (2001) annual fluxes are from an ocean inversion model constrained to a net global air-sea flux of zero. Resplandy et al. (2015) fluxes are an average of six CMIP5 models. The Subpolar South Atlantic region is from 36°S–58°S and 70°W–20°E. The Subpolar South Pacific and Subpolar South Indian region is from 36°S–58°S and 20°E–70°W. The South of 36°S and South of 58°S regions include all fluxes poleward of those latitudes. Positive fluxes are to the atmosphere.

Because Gruber et al. (2001) depends on the underlying transport model to determine fluxes, it is possible that this significant difference is partially due to differences in water mass location between the model and the actual Southern Ocean. A subsequent multimodel comparison (Resplandy et al., 2015) finds good agreement with the Gruber et al. (2001) estimates globally, though with the largest disagreement in the Subpolar South Atlantic with a flux of ~5 ± 20 Tmol yr^{-1}. Najjar and Keeling (2000) calculate the air-sea oxygen flux based on the Najjar and Keeling (1997) oxygen climatology, using surface measurements and an air-sea flux parameterization. In the Atlantic they find a sharp transition from a strong influx of oxygen (~−3.2 mol m^{-2} yr^{-1}) at ~58°S to an almost equally strong outgassing around 40°S (~2.5 mol m^{-2} yr^{-1}). The location of these opposing fluxes within the Subpolar South Atlantic region defined by Gruber et al. (2001) would greatly influence the total flux in that region. However, it is important to note that Najjar and Keeling (2000) and Gruber et al. (2001) reach conflicting conclusions regarding the pattern of global oxygen fluxes, with opposing signs in the equatorial oceans and significant differences in the subpolar regions, so regional comparisons are problematic between these two studies.

Overall, a −110 Tmol O_2 yr^{-1} change in the Southern Ocean oxygen flux to −221 Tmol O_2 yr^{-1} would put the magnitude of Southern Ocean uptake roughly equal to the equatorial (13°S–13°N) outgassing calculated in Gruber et al. (2001). In order to maintain an assumption of no net annual global air-sea oxygen flux or to match current estimates of ocean oxygen loss due to warming, increasing the Southern Ocean uptake would require additional outgassing elsewhere in the ocean.

The accuracy of the large flux estimated in this study is dependent on an adequate representation of the total region by the available Argo oxygen floats. Subsampling of CM2.6 output at the float locations indicated little offset in the STZ and PAZ regions, but a significant offset in the SAZ and SIZ (supporting information Figure S2 and Table S1). In the latter regions, the fluxes calculated from the subsampled data were more negative than the full model mean flux. Although the model representation of the spatial and temporal variability in oxygen fluxes is certainly flawed in a number of ways, this result could indicate that the float-based flux of oxygen into the ocean calculated in this study is biased high. However, even if the true magnitude of the flux is somewhat smaller, the oxygen flux into the Southern Ocean found here is still on the higher end of prior estimates and significant on a global scale. This source of uncertainty needs to be more fully understood in the future, when the true heterogeneity and variability of ocean oxygen fluxes is better known.

3.3. Processes Contributing to Air-Sea Fluxes

The total air-sea oxygen flux (equation (1)) can be separated into a thermal and a nonthermal component, where the nonthermal component includes both biological processes and physical transport fluxes:

$$F_{\text{total}} = F_{\text{thermal}} + F_{\text{non-thermal}} \tag{6}$$

Oxygen solubility is strongly temperature dependent. Using the relationship between changes in oxygen solubility and temperature and assuming instantaneous equilibration, the thermal oxygen flux can be calculated as a function of the surface heat flux (Keeling et al., 1993):

$$F_{\text{thermal}} = -\frac{dO_{2,sat}}{dT}\frac{Q}{C_p}\rho_w \tag{7}$$

where $dO_{2,sat}/dT$ (mol kg^{-1} K^{-1}) is the temperature derivative of oxygen solubility, Q (J m^{-2} s^{-1}) is the total heat flux calculated from the ECMWF ERA-Interim reanalysis surface latent, sensible, net solar radiation, and net thermal radiation 12 h heat flux estimates, and C_p (J m^{-3} K^{-1}) is the heat capacity of seawater. Modeling studies that have assessed this relationship between oxygen and heat fluxes have found that the magnitude of the calculated thermal oxygen flux can be overestimated due to the assumption of instantaneous oxygen equilibration (Jin et al., 2007). Additionally, the thermally driven oxygen fluxes may lag the heat flux by a few weeks (Manizza et al., 2012). However, these results are dependent on the air-sea flux parameterization and ocean model used and it is unclear if the relationship would be different with the modified Liang et al. (2013) parameterization used in this study. Therefore, we chose to use the unaltered Keeling et al. (1993) parameterization for our monthly estimates of thermal oxygen fluxes, though the thermal oxygen flux estimates may be slightly high in spring/early summer.

$F_{\text{non-thermal}}$ is calculated as the difference between the F_{total} and F_{thermal} fluxes. F_{thermal} was calculated at each interpolated float position and monthly means were calculated from 2008 to 2016 (Figure 7 and Table 6). In all regions, the thermal component of the oxygen flux follows the seasonal cycle of temperature, with a heat flux into the ocean during the summer warming the water, reducing the solubility and driving an outgassing of oxygen to the atmosphere. In the winter, a heat flux to the atmosphere cools the upper ocean, increasing the solubility of oxygen and driving a flux into the ocean. In the STZ, the magnitude of the thermal component of the oxygen flux is greater than 50% of the total monthly mean flux in all but 2 months. Moving southward, the significance of F_{thermal} decreases with the reduced amplitude of the seasonal temperature cycle, with F_{thermal} greater than 50% of the total oxygen flux in 8 months in the SAZ, 6 months in the PAZ, and only 3 months in the SIZ.

$F_{\text{non-thermal}}$ is largest in the summer/fall in the STZ and in the winter/spring in the SAZ, PAZ, and SIZ. With the decreased importance of F_{thermal} to the south, $F_{\text{non-thermal}}$ is calculated to be a larger fraction of the total, especially in winter months when the total oxygen flux is strongly into the ocean. The SIZ displays only a weak total outgassing of oxygen during 2 months of the year (January and February) and a relatively consistent nonthermal flux to the ocean from April to December.

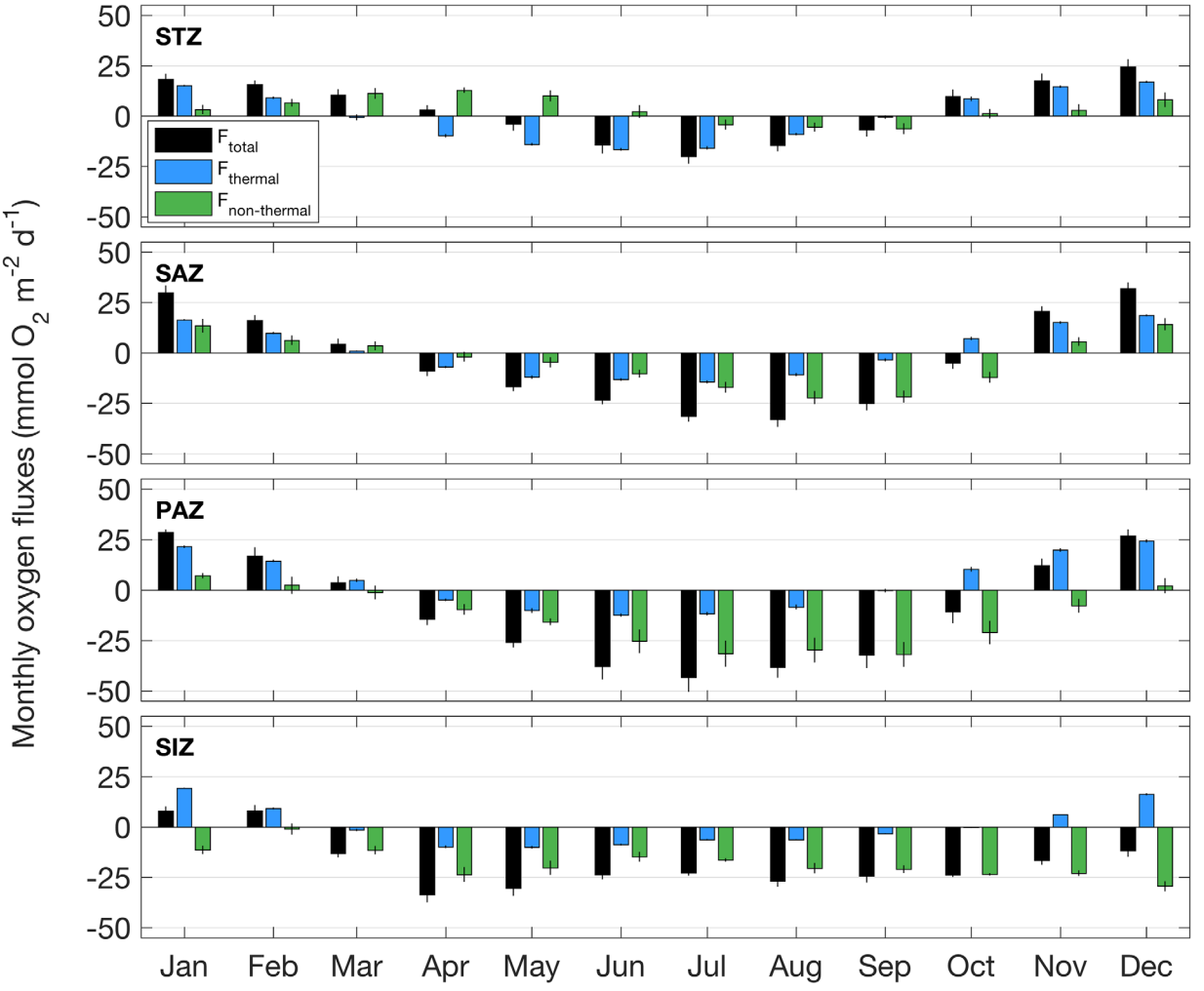

Figure 7. Monthly total, thermal, and nonthermal oxygen fluxes for each region. Monthly means of total flux (black) and thermal flux (blue) are calculated from the individual monthly means for each year. Error bars represent ±1 standard error around the mean. Nonthermal fluxes (green) are calculated as the difference between the total and thermal fluxes, with the error as the sum of total and thermal standard errors.

The mean annual thermally driven oxygen fluxes are balanced in the STZ (–0.1 ± 0.3 mol O_2 m^{-2} yr^{-1}), SAZ (0.2 ± 0.3 mol O_2 m^{-2} yr^{-1}), and SIZ (0.1 ± 0.2 mol O_2 m^{-2} yr^{-1}), but positive (net outgassing) in the PAZ (1.4 ± 0.3 mol O_2 m^{-2} yr^{-1}, Table 6). This spatial pattern of roughly zero annual net heat flux over much of the Southern Ocean but net heat uptake in the PAZ is consistent with a climatological heat flux analysis (Large & Yeager, 2009) that indicates near-zero heat fluxes south of 60°S, a band of heat uptake in the Antarctic Circumpolar Current, and a mix of heat uptake and loss between 30°S and 40°S.

In the STZ, $F_{non\text{-}thermal}$ is positive (1.3 ± 1.1 mol O_2 m^{-2} yr^{-1}), but is increasingly negative to the south (SAZ, −1.5 ± 0.9 mol O_2 m^{-2} yr^{-1}; PAZ −4.9 ± 1.4 mol O_2 m^{-2} yr^{-1}; SIZ, −6.5 ± 0.7 mol O_2 m^{-2} yr^{-1}) indicating net nonthermal uptake of oxygen by the ocean in each of these regions. The total annual thermal flux of 22 ± 2.6 Tmol O_2 yr^{-1} in the Subpolar South Atlantic region agrees well with Gruber et al. (2001) estimate of 30.5 Tmol O_2 yr^{-1} (Table 5), while the large difference in the total fluxes results in a similarly large difference in the calculated nonthermal fluxes. The agreement between the thermal fluxes is worse in the Subpolar South Indo-Pacific and south of 58°S, with greater thermal outgassing in this study for both regions, of ~29 and ~47 Tmol O_2 yr^{-1}, respectively. Given the differences in total fluxes noted above and that calculation of nonthermal fluxes is dependent on the total flux, it is difficult to draw meaningful conclusions about

Table 6
Thermal and Nonthermal Fluxes

	STZ		SAZ		PAZ		SIZ	
mmol O_2 m^{-2} d^{-1}	Thermal	Nonthermal	Thermal	Nonthermal	Thermal	Nonthermal	Thermal	Nonthermal
Jan	15 ± 0.4	3.3 ± 3.1	16 ± 0.3	13 ± 3.9	22 ± 0.6	7.1 ± 2	19 ± 0.2	−11 ± 2.6
Feb	9.1 ± 0.6	6.7 ± 2.5	9.8 ± 0.5	6.1 ± 3.3	14 ± 0.6	2.3 ± 5	9.1 ± 0.5	−1 ± 3.4
Mar	−0.7 ± 1.4	11 ± 4.2	0.8 ± 0.3	3.4 ± 3.1	4.8 ± 0.8	−1.2 ± 4	−1.5 ± 0.6	−11 ± 2.6
Apr	−9.8 ± 0.9	13 ± 3.3	−7 ± 0.6	−2 ± 3.1	−4.9 ± 0.6	−9.6 ± 3.5	−9.8 ± 0.7	−24 ± 4.7
May	−14 ± 0.7	10 ± 4.1	−12 ± 0.8	−4.7 ± 3.1	−10 ± 1.2	−16 ± 3.8	−10 ± 0.7	−20 ± 4.5
Jun	−17 ± 0.7	2.3 ± 5.1	−13 ± 0.6	−10 ± 2.7	−12 ± 0.7	−26 ± 7.2	−8.8 ± 0.4	−15 ± 2.9
Jul	−16 ± 0.9	−4.3 ± 4.4	−14 ± 0.7	−17 ± 3.4	−12 ± 0.9	−32 ± 8	−6.4 ± 0.4	−16 ± 1.9
Aug	−9 ± 0.6	−5.6 ± 3.6	−11 ± 0.7	−22 ± 4.5	−8.4 ± 1.2	−30 ± 6.4	−6.4 ± 0.3	−20 ± 3.1
Sep	−0.5 ± 0.8	−6.4 ± 4.2	−3.4 ± 0.7	−22 ± 4.2	−0.3 ± 0.9	−32 ± 7.3	−3.4 ± 0.3	−21 ± 3.5
Oct	8.6 ± 1.2	1.1 ± 4.6	7.1 ± 0.8	−12 ± 3.7	10 ± 1.2	−21 ± 6.9	−0.2 ± 0.3	−24 ± 1.4
Nov	15 ± 0.6	2.9 ± 4.3	15 ± 0.7	5.5 ± 3.1	20 ± 0.9	−7.8 ± 4.3	6.2 ± 0	−23 ± 2.2
Dec	17 ± 0.5	7.7 ± 4.2	19 ± 0.4	13 ± 3.5	24 ± 0.8	2.6 ± 4	16 ± 0.5	−28 ± 3.5
Mean annual (mol O_2 m^{-2} yr^{-1})	−0.1 ± 0.3	1.3 ± 1.1	0.2 ± 0.3	−1.5 ± 0.9	1.4 ± 0.3	−4.9 ± 1.4	0.1 ± 0.2	−6.5 ± 0.7

Note. Thermal and nonthermal monthly and mean annual fluxes for the four provinces used in this study calculated according to equations (6) and (7). Thermal fluxes are the oxygen flux due to temperature changes associated with air-sea heat fluxes. Nonthermal fluxes include both biology and mixing.

the agreement or disagreement in nonthermal fluxes between this study and Gruber et al. (2001). However, differences in the thermal component of the flux in the Subpolar South Indo-Pacific and south of 58°S indicate differences between the heat flux estimates from the ocean inversion model and those calculated from the ECMWF product that could be due to biases in either model, interannual/interdecadal variability, or both.

In much of our current analysis we have averaged data into one annual year in order to provide our best estimate of the mean state and reduce uncertainty and variance around that mean. Plotting the cumulative fluxes over the 9 years of data gives an indication of the amount of variability in the total, thermal, and nonthermal fluxes for each province (Figure 8). Significant variability is present in both the amplitude of the seasonal cycles and in the total annual fluxes. The Southern Ocean is undergoing significant changes in oxygen content (Schmidtko et al., 2017) and ventilation (Waugh et al., 2013), making it important to realize that the annual means we calculate obscure some of these changes and may be biased relative to a mean made over several decades. A significant feature in both the SAZ and the PAZ is an anomalous influx of oxygen during the winter of 2013. This appears to be roughly correlated with a deeper than usual mixed layer depth during that time (not shown) but the direct cause is not clear. With almost a decade of continuous observations, a future in depth analysis of interannual variability should now be possible and is the focus of future work.

In Manizza et al. (2012), modeled global air-sea oxygen fluxes were assessed to understand the importance and timing of biology and ventilation to the total nonthermal flux. In the Southern Ocean (>30°S), they found that during the summertime, ventilation is only ∼10% of the total oxygen flux, and that the majority of the nonthermal flux during summer months was due to biology. Ventilation always drove a negative flux into the ocean and was the strongest contributor to the nonthermal flux during the winter, while both biology and ventilation were important in the spring. From this, we can conclude that the net positive nonthermal flux in the STZ indicates that net annual biological production is driving the outgassing signal, while the net negative $F_{\text{non-thermal}}$ in the SAZ, PAZ, and SIZ are due to an increasing ventilation signal to the south.

To further understand the nonthermal component of the regional oxygen fluxes, we analyzed the relationship between the nonthermal oxygen fluxes and net primary production (NPP) and mixed layer depth for each region as proxies for the biological and ventilation processes that impact the air-sea oxygen flux. The nonthermal component for each month in the time series was plotted against monthly averaged NPP for the same region from the carbon-based productivity model (CbPM, Westberry et al., 2008, monthly data

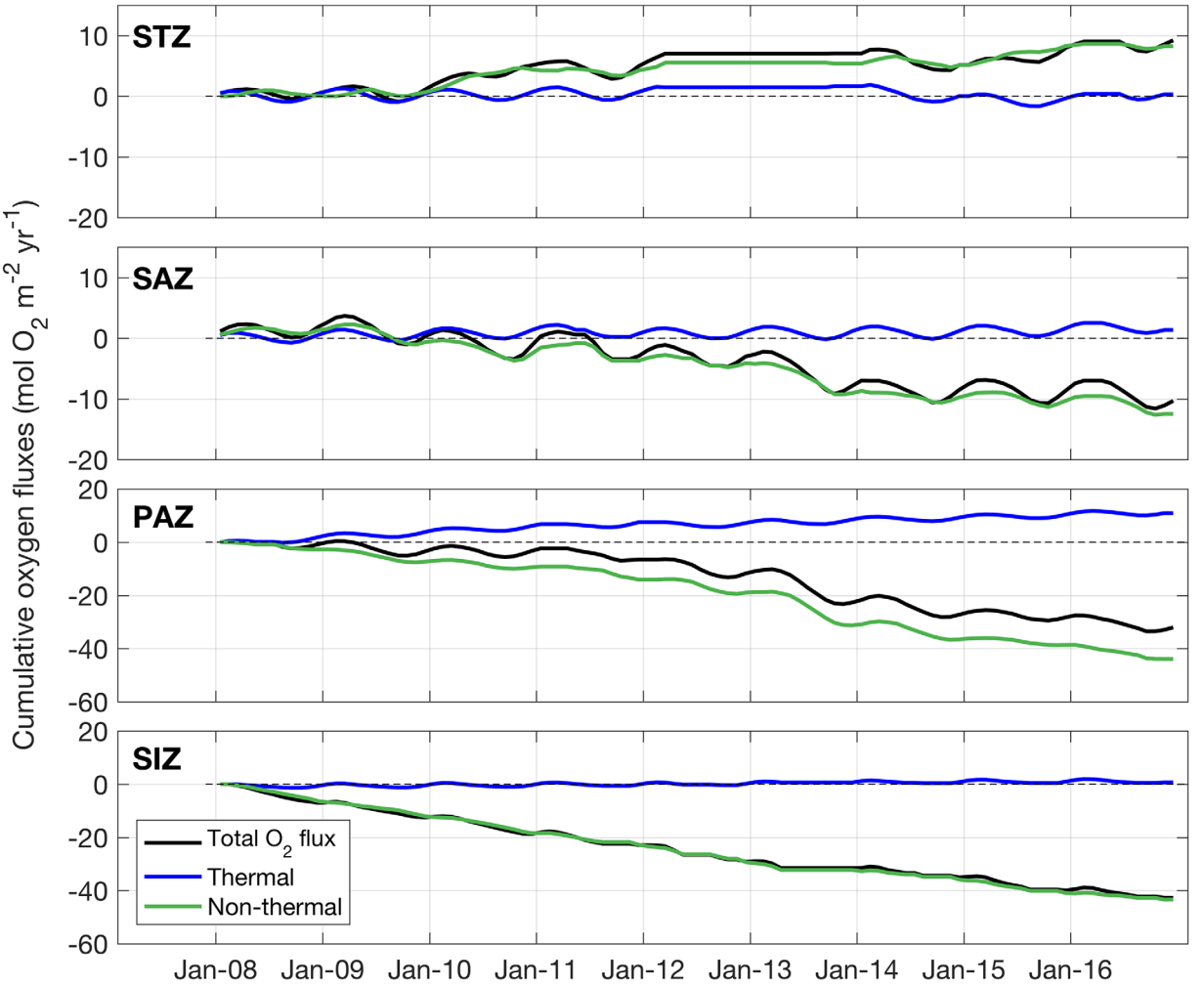

Figure 8. Cumulative total, thermal, and nonthermal oxygen fluxes from 2008 to 2016. Cumulative fluxes are calculated from the sum of the individual months to represent the long-term balance of fluxes in each region. Flat areas in the cumulative flux lines correspond to months removed from analysis due to incomplete float coverage. The *y* axis limits are different for the STZ/SAZ and PAZ/SIZ in order to better show variability in the seasonal cycles.

downloaded from www.science.oregonstate.edu/ocean.productivity/) and against float-derived mixed layer depth (Figure 9). NPP estimates from satellite data can be biased in polar regions by poor satellite coverage and newer estimates of NPP may better account for photosynthetic production below shallow mixed layers (Silsbe et al., 2016), but the available CbPM NPP product is a useful starting point for identifying the relationship between primary production and the nonthermal oxygen flux. Similarly, mixed layer depth does not exactly equate to ventilation, but does indicate the fraction of the water column exposed to the atmosphere for each month, with deeper mixed layer depths entraining more low-oxygen water from below.

Model I regressions and the associated regression coefficients (R^2) indicate the fraction of variance in the nonthermal oxygen flux explained by NPP and mixed layer depth (Figure 9). The color of each point indicates the month of the year, with summer months dark colors and winter months lighter. NPP should result in production of oxygen and an associated outgassing whereas deepening mixed layers will entrain water deficient in oxygen and drive an uptake of oxygen by the ocean. The nonthermal flux is positively correlated with NPP and negatively correlated with mixed layer depth in the STZ, SAZ, and PAZ. The nonthermal flux in the SIZ is not correlated with either NPP or mixed layer depth. The largest fraction of variance explained is in the SAZ by the mixed layer depth, consistent with the deep upwelling observed in this region. While the relationship with MLD explains a greater fraction of the variance in the three northern regions than NPP, care must be taken in assigning the relative importance of primary production and entrainment given the relationship and correlation between NPP and MLD.

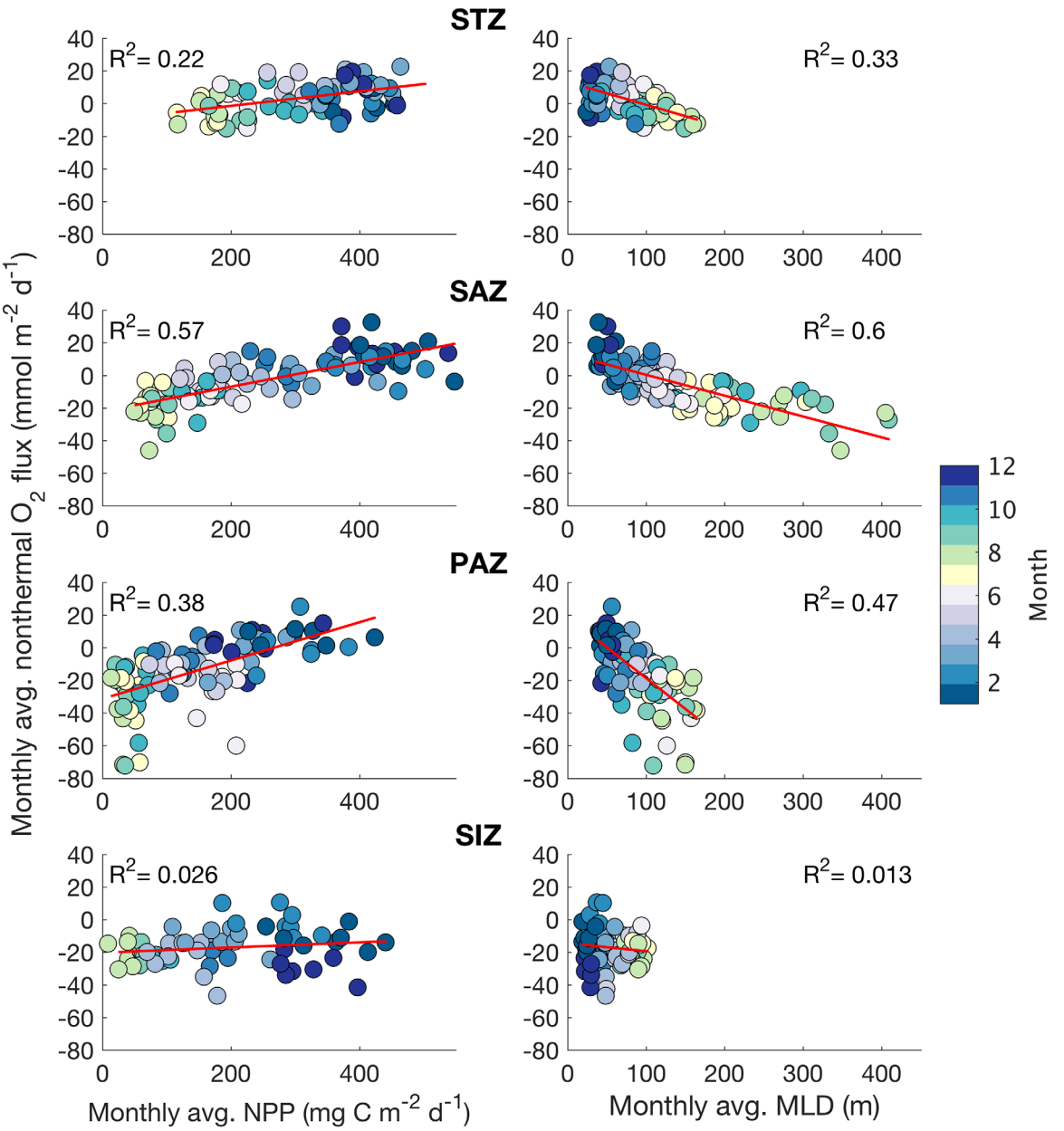

Figure 9. Correlations between monthly nonthermal oxygen fluxes, net primary production (NPP), and mixed layer depth (MLD). Monthly mean nonthermal oxygen fluxes for each region plotted against (left column) CbPM net primary production (NPP) and (right column) monthly mean MLD. Points are colored according to month, with lighter colors representing wintertime and darker colors representing summertime. Model I regressions were fit to each set of data (red line, R^2 = fraction of *y* variance explained by the *x* variable).

During summer months, shallow mixed layers increase the available light for photosynthesis, while available nutrients from the previous winters' deep mixing and warming waters drive an increase in primary production. As mixed layers deepen in the late summer and fall, the entrained water is often initially higher in oxygen than the mixed layer, due to the isolation of the submixed layer waters from the atmosphere and the higher temperatures in the summertime mixed layer. When mixed layers deepen further, low-oxygen water is entrained, contributing to the wintertime flux of oxygen into the ocean. These processes combine to give the strong relationships between the nonthermal oxygen flux and both NPP and MLD.

The lack of correlation in the SIZ could be due to the restriction of the air-sea oxygen flux by sea ice during much of the year. Mixed layer changes and the associated entrainment of low-oxygen waters could still drive the large observed air-sea flux but would be decoupled from that particular month's total oxygen flux.

Advection of the low-oxygen waters of the SIZ northward would also contribute to the net oxygen influx in the PAZ. Uncertainties in sea-ice fraction or the scaling of gas flux with sea-ice fraction could significantly impact this part of the seasonal flux, as described in the next section.

3.4. Seasonal Ice Zone Oxygen Flux

The SIZ is characterized by a strong oxygen flux into the ocean. Data in this region have been previously scarce, especially during winter months (Figure 1c), but gridded climatologies and model output can be compared to our results. The World Ocean Atlas (WOA) (Garcia et al., 2010) is a gridded data set of shipboard measurements of oxygen concentrations and supersaturations. In the Southern Ocean, these data are biased toward summer months, due to the difficulty of conducting shipboard operations during winter conditions. Binning and averaging the float oxygen supersaturation (supersaturation $= \{([O_2]_{measured} - [O_2]_{saturation})/[O_2]_{saturation}\} \times 100$) by month shows good agreement with WOA for the STZ, SAZ, and PAZ, but diverges from WOA mean supersaturations from July to October in the SIZ (supporting information Figure S3). Mean September oxygen supersaturation from Argo floats in the SIZ is $-14.3 \pm 6.6\%$, while mean WOA supersaturation from the same region is less than 2/3 the magnitude, at $-8.6 \pm 6.6\%$.

The boundaries of the SIZ are similar to the Gruber et al. (2001) region poleward of 58°S and, as noted earlier, their estimate of -136.8 Tmol O_2 yr^{-1} for 58°S is fairly close to our estimate of -167 ± 19 Tmol O_2 yr^{-1} in this region (Figure 6). However, in their initial model estimate unconstrained to a net global zero air-sea oxygen flux, they calculated an uptake of only -76.6 Tmol O_2 yr^{-1}. The change in calculated fluxes between the unconstrained and constrained ocean inversions was greater in the Southern Ocean than in any of the other regions they studied. This is likely due to the relative lack of observations in the Southern Ocean, giving the model the most flexibility to adjust the air-sea flux output in the region. An updated ocean inversion model incorporating global Argo oxygen measurements may be able to accurately calculate air-sea fluxes in the Southern Ocean without the addition of external constraints. Oxygen fluxes in the SIZ region from climate models yield annual values that range from similar in magnitude to ours (Bopp et al. (2002), ~ -130 Tmol O_2 yr^{-1}, calculated from an estimate of -5 mol O_2 m^{-2} yr^{-1} >58°S in Figure 5), to similar values as the unconstrained Gruber et al. (2001) result (Resplandy et al., 2015; ~ -83 Tmol O_2 yr^{-1}, estimated from Figure 2). Najjar and Keeling (2000) set the air-sea fluxes in ice-covered regions to zero, making comparison with this study difficult.

Because our annual SIZ oxygen fluxes are on the upper end of the range of model and data-based estimates, it is worth evaluating the sensitivity of our results to choices in flux parameterization or exchange through fractional sea ice. Recalculating air-sea exchange with the Wanninkhof (2014) gas exchange parameterization yields only a relatively small change of -0.6 mol O_2 m^{-2} yr^{-1} in the SIZ, making it unlikely that this result is due to gas parameterization choice.

New observations of significantly undersaturated waters in the SIZ do not, by themselves, indicate a strong influx of oxygen during the winter. The undersaturated waters must be able to exchange with the atmosphere in order for that to happen. Gas exchange through sea ice is not well constrained. Many models use the linear scaling described in section 2.4 (McNeil et al., 2007) or a similar approach (e.g., Takahashi et al., 2009; assume that gas exchange is unaffected by ice from 0 to 10% sea-ice cover, and that it scales linearly with ice cover between 10 and 90%, with maximum sea-ice cover fixed at 90% to account for intermittent cracks and openings). Targeted studies indicate that the true exchange through fractional sea ice may be up to an order of magnitude lower than would be the case if there were a linear relationship to sea-ice fraction (Rutgers van der Loeff et al., 2014), but this remains a topic of on-going research.

As a test of the sensitivity of our SIZ gas exchange to the sea-ice fraction air-sea flux scaling, we recalculated the SIZ flux using a linear scaling from 0 to 50% and allowing no exchange when the ice fraction was >50%, an approach mentioned in McNeil et al. (2007). This resulted in a mean flux of -3.1 ± 1.0 mol O_2 m^{-2} yr^{-1}, indicating that over half of the total exchange in the SIZ is in waters covered by over 50% ice. The sensitivity of this result to the reduction in air-sea exchange by sea ice points to the need for a more robust parameterization of gas exchange in regions seasonally covered by ice. Integration of this new float data into our understanding of the Southern Ocean, either through inversion models or simpler mass balance approaches, should help to determine the true flux of oxygen through fractional sea ice. Variability in the amount of low-oxygen waters supplied by deep convective upwelling in this region may also introduce greater uncertainty to the mean flux (Resplandy et al., 2015).

4. Summary

In most areas of the ocean, oxygen has historically been measured only on decadal repeat hydrography cruises. Global ocean estimates of air-sea oxygen fluxes were possible from data climatologies (Garcia & Keeling, 2001; Gruber et al., 2001; Najjar & Keeling, 2000), but sparse oxygen measurements, especially in the Southern Ocean, and uncertainty in the air-sea transfer velocities were primary sources of error (Najjar & Keeling, 2000). The introduction of oxygen sensors onto Argo floats adds important constraints to our understanding of the temporal and spatial variability of the ocean oxygen cycle. While sensor drift before deployment initially prevented use of these sensors in applications that required high absolute accuracy, recent advances in the methods of reanalysis of old data and newly deployed air-calibrated floats through SOCCOM have the ability to supplement and enhance the cruise data records, yielding new insights into the seasonal cycles of oxygen concentrations. In addition, improvements in air-sea flux parameterizations for less soluble gases have now given us greater confidence in our ability to calculate oxygen fluxes from the Argo array. Comparison of the new Argo float data and cruise data shows these measurements have good agreement and can be used in an analysis of multiyear air-sea fluxes of oxygen.

A large fraction of this increased uptake is due to strongly undersaturated waters in the seasonally ice-covered region where measurements have been particularly scarce in the past. Our analysis of the thermal and nonthermal components of the oxygen flux indicate that biological production is responsible for outgassing in the STZ, while upwelling of deep, oxygen deficient waters dominates the SAZ, PAZ, and SIZ.

The largest source of uncertainty in the land and carbon sink partitioning in analyses of atmospheric potential oxygen (APO, (Stephens et al., 1998)) that use the stoichiometric ratios of oxygen and carbon in fossil fuel emissions and land uptake to determine the fate of anthropogenic carbon is the uncertainty in the air-sea oxygen flux (Manning & Keeling, 2006). An increase in the Southern Ocean oxygen sink of $\sim$100 Tmol O_2 yr^{-1} would greatly impact interpretation of atmospheric measurements. While significant uncertainty remains in the air-sea flux through fractional sea ice, $\sim$70% of the total Southern Ocean flux is through open water or a sea-ice fraction of less than 50% and would be largely unaffected by a change in the sea-ice gas flux parameterization.

A larger Southern Ocean uptake of oxygen would also be important to interpretations of the latitudinal gradient in APO. A tropical "bulge" is observed in APO that represents a gradient between outgassing in the tropics and uptake at the poles (Battle et al., 2006; Gruber et al., 2001). Greater uptake of oxygen in the Southern Ocean would increase the tropical bulge and have a significant impact on the comparison between modeled representations of APO and observations.

Characterization of the mean state and interannual variability requires air-sea flux estimates of a decade or longer (Nevison et al., 2008), which we are currently on the threshold of achieving. Additional float measurements will also help to reduce any possible biases in air-sea flux estimates due to undersampling in space. Furthermore, long-term measurements are required to better resolve ocean oxygen changes due to warming and stratification. Globally, the oxygen loss due to climate change is estimated to be an outgassing of $\sim$25 to 55 Tmol O_2 yr^{-1} (Helm et al., 2011; Ito et al., 2017; Keeling et al., 2010; Manning & Keeling, 2006). The Southern Ocean is responsible for a large portion of this loss (Schmidtko et al., 2017) and is predicted to experience some of the largest future changes (Matear et al., 2000).

Observed and predicted expansion of oxygen minimum zones and decrease in ocean oxygen content make it critical to understand the air-sea flux of oxygen and the ventilation of the ocean interior (Keeling et al., 2010; Stramma et al., 2010). As expansion of the Argo oxygen data set allows better global quantification of long-term mean oxygen and trends, we will improve our ability to constrain and interpret atmospheric observations and detect ocean oxygen trends that should already be present (Long et al., 2016) and that are predicted for the future.

Acknowledgments
SOCCOM float data were collected and made freely available by the Southern Ocean Carbon and Climate Observations and Modeling (SOCCOM) Project funded by National Science Foundation, Division of Polar Programs (NSF PLR -1425989), supplemented by NOAA and NASA (PI Jorge Sarmiento). We would like to thank R. Drucker and S. Riser for providing the University of Washington Argo data set (v1.1, supported from NOAA grant NA15OAR4320063 to the University of Washington). We would also like to thank the many people at the Monterey Bay Aquarium Research Institute and the University of Washington who quality controlled and corrected the SOCCOM float data. SOCCOM data used in this analysis can be found in a data snapshot taken on 6 June 2017 (http://soccompu.princeton.edu/www/index.html, https://doi.org/10.6075/J0348H8K). NOAA High-Resolution SST data provided by the NOAA/OAR/ESRL PSD, Boulder, Colorado, USA, from their Web site at http://www.esrl.noaa.gov/psd/. We would like to thank the Argo program, without which none of this research is possible. Argo temperature and salinity for the floats in this study are available at http://www.seanoe.org/data/00311/42182/ (Argo, 2000). SOCCOM cruise data and deployment information available at: https://soccom.princeton.edu/content/ship-board-data-reports. We thank J. Plant for SOCCOMviz ingestion scripts. Rick Slater provided CM2.6 monthly output and subsampled daily model oxygen fluxes at float locations. We would especially like to thank the numerous scientists and ship's crews involved in the deployment, collection, and quality control of the data used in this study. Finally, we would like to thank Nicolas Gruber and an anonymous reviewer for their helpful comments that greatly improved this manuscript.

References

Aoki, S., Bindoff, N. L., & Church, J. A. (2005). Interdecadal water mass changes in the Southern Ocean between 30°E and 160°E. *Geophysical Research Letters*, *32*, L07607. https://doi.org/10.1029/2004GL022220

Argo. (2000). *Argo float data and metadata from Global Data Assembly Centre (Argo GDAC)*. SEANOE. https://doi.org/10.17882/42182

Battle, M., Fletcher, S. M., Bender, M. L., Keeling, R. F., Manning, A. C., Gruber, N., . . . Paplawsky, B. (2006). Atmospheric potential oxygen: New observations and their implications for some atmospheric and oceanic models. *Global Biogeochemical Cycles*, *20*(1), GB1010. http://doi.org/10.1029/2005GB002534

Bittig, H. C., & Körtzinger, A. (2015). Tackling oxygen optode drift: Near-surface and in-air oxygen optode measurements on a float provide an accurate in-situ reference. *Journal of Atmospheric and Oceanic Technology*, *32*(8), 1536–1543. https://doi.org/10.1175/JTECH-D-14-00162.1

Bittig, H. C., & Körtzinger, A. (2017). Technical note: Update on response times, in-air measurements, and in situ drift for oxygen optodes on profiling platforms. *Ocean Science*, *13*(1), 1–11. https://doi.org/10.5194/os-2016-75

Bopp, L., Le Que, C., Heimann, M., Manning, A. C., & Monfray, P. (2002). Climate-induced oceanic oxygen fluxes: Implications for the contemporary carbon budget. *Global Biogeochemical Cycles*, *16*(2). https://doi.org/10.1029/2001GB001445

Bushinsky, S. M., & Emerson, S. (2013). A method for in-situ calibration of Aanderaa oxygen sensors on surface moorings. *Marine Chemistry*, *155*, 22–28. https://doi.org/10.1016/j.marchem.2013.05.001

Bushinsky, S. M., & Emerson, S. R. (2015). Marine biological production from in situ oxygen measurements on a profiling float in the Subarctic Pacific Ocean. *Global Biogeochemical Cycles*, *29*, 2050–2060, https://doi.org/10.1002/2015GB005251

Bushinsky, S. M., Emerson, S. R., Riser, S. C., & Swift, D. D. (2016). Accurate oxygen measurements on modified Argo floats using in situ air calibrations. *Limnology and Oceanography Methods*, *14*, 491–505. https://doi.org/10.1002/lom3.10107

Cavalieri, D. J., Parkinson, C. L., Gloersen, P., & Zwally, H. J. (1996). Sea ice concentrations from Nimbus-7 SMMR and DMSP SSM/I-SSMIS passive microwave data, version 1. Boulder, CO: NASA National Snow and Ice Data Center. https://doi.org/10.5067/8GQ8LZQVL0VL

D'Asaro, E. A., & McNeil, C. (2013). Calibration and stability of oxygen sensors on autonomous floats. *Journal of Atmospheric and Oceanic Technology*, *30*(8), 1896–1906. https://doi.org/10.1175/JTECH-D-12-00222.1

de Boyer Montégut, C., Madec, G., Fischer, A. S., Lazar, A., & Iudicone, D. (2004). Mixed layer depth over the global ocean: An examination of profile data and a profile-based climatology. *Journal of Geophysical Research*, *109*, C12003. https://doi.org/10.1029/2004JC002378

Dee, D. P., Uppala, S. M., Simmons, A. J., Berrisford, P., Poli, P., Kobayashi, S., . . . Vitart, F. (2011). The ERA-interim reanalysis: Configuration and performance of the data assimilation system. *Quarterly Journal of the Royal Meteorological Society*, *137*(656), 553–597. https://doi.org/10.1002/qj.828

Delworth, T. L., A. Rosati, W. Anderson, A.J. Adcroft, V. Balaji, R. Benson, . . . Zhang, R. (2012). Simulated climate and climate change in the GFDL CM2.5 high-resolution coupled climate model. *Journal of Climate*, *25*(8), 2755–2781. https://doi.org/10.1175/JCLI-D-11-00316.1

Drucker, R., & Riser, S. C. (2016). In situ phase-domain calibration of oxygen Optodes on profiling floats. *Methods in Oceanography*, *17*(November), 1–34. https://doi.org/10.1016/j.mio.2016.09.007

Emerson, S., & Bushinsky, S. (2014). Oxygen concentrations and biological fluxes in the open ocean. *Oceanography*, *27*(1), 168–171. https://doi.org/10.5670/oceanog.2014.20

Emerson, S. R., & Bushinsky, S. (2016). The role of bubbles during air-sea gas exchange. *Journal of Geophysical Research: Ocean*, *121*, 4360–4376. https://doi.org/10.1002/2016JC011744

Fairall, C. W., Yang, M., Bariteau, L., Edson, J. B., Helmig, D., McGillis, W., . . . Blomquist, B. (2011). Implementation of the coupled ocean-atmosphere response experiment flux algorithm with CO_2, dimethyl sulfide, and O_3. *Journal of Geophysical Research*, *116*, C00F09. https://doi.org/10.1029/2010JC006884

Fiedler, B., Fietzek, P., Vieira, N., Silva, P., Bittig, H. C., & Körtzinger, A. (2013). In situ CO_2 and O_2 measurements on a profiling float. *Journal of Atmospheric and Oceanic Technology*, *30*(1), 112–126. https://doi.org/10.1175/JTECH-D-12-00043.1

Galbraith, E. D., Dunne, J. P., Gnanadesikan, A., Slater, R. D., Sarmiento, J. L., Dufour, C. O., . . . Marvasti, S. S. (2015). Complex functionality withminimal computation: Promise and pitfalls of reduced-tracer ocean biogeochemistry models. *Journal of Advances in Modeling Earth Systems*, *7*, 2012–2028. https://doi.org/10.1002/2015MS000463

Galbraith, E. D., Gnanadesikan, A., Dunne, J. P., & Hiscock, M. R. (2010). Regional impacts of iron-light colimitation in a global biogeochemical model. *Biogeosciences*, *7*, 1043–1064. https://doi.org/10.5194/bgd-6-7517-2009

García, H. E., & Gordon, L. I. (1992). Oxygen solubility in seawater: Better fitting equations. *Limnology and Oceanography*, *37*(6), 1307–1312. https://doi.org/10.4319/lo.1992.37.6.1307

Garcia, H. E., & Keeling, R. F. (2001). On the global oxygen anomaly and air-sea flux. *Journal of Geophysical Research*, *106*(C12), 31155–31166. https://doi.org/10.1029/1999JC000200

Garcia, H. E., Locarnini, R. A., Boyer, T. P., Antonov, J. I., Baranova, O. K., Zweng, M. M., & Johnson, D. R. (2010). *World Ocean Atlas 2009 Volume 3: Dissolved Oxygen, Apparent Oxygen Utilization, and Oxygen Saturation*. S. Levitus (Ed.), *NOAA Atlas NESDIS 70* (344 pp.). Washington, DC: U.S. Government Printing Office.

Gruber, N., Doney, S. C., Emerson, S., Gilbert, R., Kobayashi, D., Körtzinger, T. A., . . . Ulloa, O. (2009). Adding oxygen to Argo: Developing a global in-situ observatory for ocean deoxygenation and biogeochemistry. Paper presented at Ocean Obs '09: Sustained ocean observations and information for society, Venice, Italy.

Gruber, N., Gloor, M., Fan, S.-M., & Sarmiento, J. L. (2001). Air-sea flux of oxygen estimated from bulk data: Implications For the marine and atmospheric oxygen cycles. *Global Biogeochemical Cycles*, *15*(4), 783–803. https://doi.org/10.1029/2000GB001302

Helm, K. P., Bindoff, N. L., & Church, J. A. (2011). Observed decreases in oxygen content of the global ocean. *Geophysical Research Letters*, *38*, L23602. https://doi.org/10.1029/2011GL049513

Ito, T., & Deutsch, C. (2010). A conceptual model for the temporal spectrum of oceanic oxygen variability. *Geophysical Research Letters*, *37*, L03601. https://doi.org/10.1029/2009GL041595

Ito, T., Minobe, S., Long, M. C., & Deutsch, C. (2017). Upper ocean O_2 trends: 1958–2015. *Geophysical Research Letters*, *44*, 4214–4223. https://doi.org/10.1002/2017GL073613

Jin, X., Najjar, R. G., Louanchi, F., & Doney, S. C. (2007). A modeling study of the seasonal oxygen budget of the global ocean. *Journal of Geophysical Research*, *112*, C05017. https://doi.org/10.1029/2006JC003731

Johnson, K. S., Plant, J. N., Coletti, L. J., Jannasch, H. W., Sakamoto, C. M., Riser, S. C., . . . Williams, N. L. (2017a). Chemical sensor performance in the SOCCOM profiling float array. *Journal of Geophysical Research: Ocean*, *122*, 6416–6436. https://doi.org/10.1002/2017JC012838

Johnson, K. S., Plant, J. N., Riser, S. C., & Gilbert, D. (2015). Air oxygen calibration of oxygen optodes on a profiling float array. *Journal of Atmospheric and Oceanic Technology*, *32*(11), 2160–2172. https://doi.org/10.1175/JTECH-D-15-0101.1

Johnson, K. S., Riser, S. C., Boss, E. S., Talley, L. D., Sarmiento, J. L., Swift, D. D., . . . Russell, J. L. (2017b). SOCCOM float data—Snapshot 2017-06-06. In *Southern Ocean Carbon and Climate Observations and Modeling (SOCCOM) float data archive* (digital collections). San Diego, CA: UC San Diego Library. https://doi.org/10.6075/J0348H8K

Keeling, R. E., Körtzinger, A., & Gruber, N. (2010). Ocean deoxygenation in a warming world. *Annual Review of Marine Science*, *2*(1), 199–229. https://doi.org/10.1146/annurev.marine.010908.163855

Keeling, R. F., & Garcia, H. E. (2002). The change in oceanic O_2 inventory associated with recent global warming. *Proceedings of the National Academy of Sciences of the United States of America*, *99*(12), 7848–7853. https://doi.org/10.1073/pnas.122154899

Keeling, R. F., Najjar, R. P., Bender, M. L., & Tans, P. P. (1993). What atmospheric oxygen measurements can tell us about the global carbon cycle. *Global Biogeochemical Cycles*, *7*(1), 37–67. https://doi.org/10.1029/92GB02733

Key, R. M., Olsen, A., van Heuven, S., Lauvset, S. K., Velo, A., Lin, X., . . . Suzuki, T. (2015). *Global ocean data analysis project, version 2 (GLODAPv2)* (Rep. ORNL/CDIAC-162, NDP-093). Oak Ridge, TN: Oak Ridge National Laboratory. https://doi.org/10.3334/CDIAC/OTG.NDP093_GLODAPv2

Large, W. G., & Yeager, S. G. (2009). The global climatology of an interannually varying air—Sea flux data set. *Climate Dynamics*, *33*(2–3), 341–364. https://doi.org/10.1007/s00382-008-0441-3

Liang, J.-H., Deutsch, C., McWilliams, J. C., Baschek, B., Sullivan, P. P., & Chiba, D. (2013). Parameterizing bubble-mediated air-sea gas exchange and its effect on ocean ventilation. *Global Biogeochemical Cycles*, *27*, 894–905. https://doi.org/10.1002/gbc.20080

Liss, P. S., & Merlivat, L. (1986). Air-sea gas exchange rates: Introduction and synthesis. In P. Buat-Ménard (Ed.), *The role of air-sea exchange in geochemical cycling* (pp. 113–127). Dordrecht, the Netherlands: D. Reidel Publishing Co.

Long, M. C., Deutsch, C., & Ito, T. (2016). Finding forced trends in oceanic oxygen. *Global Biogeochemical Cycles*, *30*, 381–397, https://doi.org/10.1002/2015GB005310

Manizza, M., Keeling, R. F., & Nevison, C. D. (2012). On the processes controlling the seasonal cycles of the air–sea fluxes of O_2 and N_2O: A modelling study. *Tellus, Series B*, *64*(August), 1–6. https://doi.org/10.3402/tellusb.v64i0.18429

Manning, A. C., & Keeling, R. F. (2006). Global oceanic and land biotic carbon sinks from the Scripps atmospheric oxygen flask sampling network. *Tellus, Series B*, *58*, 95–116. https://doi.org/10.1111/j.1600-0889.2006.00175.x

Maslanik, J., & Stroeve, J. (1999). *Near-real-time DMSP SSMIS daily polar gridded sea ice concentrations, version 1*. Boulder, CO: National Snow and Ice Data Center. Retrieved from http://nsidc.org/data/NSIDC-0081/versions/1; https://doi.org/10.5067/U8C09DWVX9LM

Matear, R. J., Hirst, A. C., & McNeil, B. I. (2000). Changes in dissolved oxygen in the Southern Ocean with climate change. *Geochemistry, Geophysics, Geosystems*, *1*(11), 1050. https://doi.org/10.1029/2000GC000086

McNeil, B. I., Metzl, N., Key, R. M., Matear, R. J., & Corbiere, A. (2007). An empirical estimate of the Southern Ocean air-sea CO_2 flux. *Global Biogeochemical Cycles*, *21*, GB3011. https://doi.org/10.1029/2007GB002991

Najjar, R. G., & Keeling, R. F. (1997). Analysis of the mean annual cycle of the dissolved oxygen anomaly in the World Ocean. *The Journal of Marine Research*, *55*(1), 117–151. https://doi.org/10.1357/0022240973224481

Najjar, R. G., & Keeling, R. F. (2000). Mean annual cycle of the air-sea oxygen flux: A global view. *Global Biogeochemical Cycles*, *14*(2), 573–584. https://doi.org/10.1029/1999GB900086

Nevison, C. D., Mahowald, N. M., Doney, S. C., Lima, I. D., & Cassar, N. (2008). Impact of variable air-sea O_2 and CO_2 fluxes on atmospheric potential oxygen (APO) and land-ocean carbon sink partitioning. *Biogeosciences*, *5*, 875–889. http://doi.org/10.5194/bg-5-875-2008

Nevison, C. D., Keeling, R. F., Kahru, M., Manizza, M., Mitchell, B. G., & Cassar, N. (2012). Estimating net community production in the Southern Ocean based on atmospheric potential oxygen and satellite ocean color data. *Global Biogeochemical Cycles*, *26*(1), GB1020. http://doi.org/10.1029/2011GB004040

Olsen, A., Key, R. M., van Heuven, S., Lauvset, S. K., Velo, A., Lin, X., . . . Suzuki, T. (2016). The global ocean data analysis project version 2 (GLODAPv2)—An internally consistent data product for the world ocean. *Earth System Science Data*, *8*(2), 297–323. https://doi.org/10.5194/essd-8-297-2016

Orsi, A. H., Whitworth, T., & Nowlin, W. D. (1995). On the meridional extent and fronts of the Antarctic Circumpolar Current. *Deep Sea Research Part I: Oceanographic Research Papers*, *42*(5), 641–673. https://doi.org/10.1016/0967-0637(95)00021-W

Plattner, G.-K., Joos, F., & Stocker, T. (2002). Revision of the global carbon budget due to changing air-sea oxygen fluxes. *Global Biogeochemical Cycles*, *16*(4), 1096. https://doi.org/10.1029/2001GB001746

Pollard, R. T., Lucas, M. I., & Read, J. F. (2002). Physical controls on biogeochemical zonation in the Southern Ocean. *Deep Sea Research Part II: Topical Studies in Oceanography*, *49*(16), 3289–3305. https://doi.org/10.1016/S0967-0645(02)00084-X

Resplandy, L., Séférian, R., & Bopp, L. (2015). Natural variability of CO_2 and O_2 fluxes: What can we learn from centuries-long climate models simulations? *Journal of Geophysical Research: Ocean*, *120*, 384–404. https://doi.org/10.1002/2014JC010463

Roemmich, D., & Gilson, J. (2009). The 2004–2008 mean and annual cycle of temperature, salinity, and steric height in the global ocean from the Argo Program. *Progress in Oceanography*, *82*(2), 81–100. https://doi.org/10.1016/j.pocean.2009.03.004

Rutgers van der Loeff, M. M., Cassar, N., Nicolaus, M., Rabe, B., & Stimac, I. (2014). The influence of sea ice cover on air-sea gas exchange estimated with radon-222 profiles. *Journal of Geophysical Research: Oceans*, *119*, 2735–2751. https://doi.org/10.1002/2013JC009321

Schmidtko, S., Stramma, L., & Visbeck, M. (2017). Decline in global oceanic oxygen content during the past five decades. *Nature*, *542*(7641), 335–339. https://doi.org/10.1038/nature21399

Silsbe, G. M., Behrenfeld, M. J., Halsey, K. H., Milligan, A. J., & Westberry, T. K. (2016). The CAFE model: A net production model for global ocean phytoplankton. *Global Biogeochemical Cycles*, *30*, 1756–1777. https://doi.org/10.1002/2016GB005521

Stanley, R. H. R., Jenkins, W. J., Lott, D. E., & Doney, S. C. (2009). Noble gas constraints on air-sea gas exchange and bubble fluxes. *Journal of Geophysical Research*, *114*, C11020, https://doi.org/10.1029/2009JC005396

Stephens, B. B., Keeling, R. F., Heimann, M., Six, K. D., Murnane, R., & Caldeira, K. (1998). Testing global ocean carbon cycle models using measurements of atmospheric O_2 and CO_2 concentration. *Global Biogeochemical Cycles*, *12*(2), 213–230. https://doi.org/10.1029/97GB03500

Stramma, L., Schmidtko, S., Levin, L. A., & Johnson, G. C. (2010). Ocean oxygen minima expansions and their biological impacts. *Deep-Sea Research Part I: Oceanographic Research Papers*, *57*(4), 587–595. https://doi.org/10.1016/j.dsr.2010.01.005

Takahashi, T., *et al.* (2009). Climatological mean and decadal change in surface ocean pCO2, and net sea-air CO2 flux over the global oceans. *Deep Sea Research Part II: Topical Studies in Oceanography*, *56*(8–10), 554–577. https://doi.org/10.1016/j.dsr2.2008.12.009

Takeshita, Y., Martz, T. R., Johnson, K. S., Plant, J. N., Gilbert, D., Riser, S. C., . . . Tilbrook, B. (2013). A climatology-based quality control procedure for profiling float oxygen data. *Journal of Geophysical Research: Ocean*, *118*, 5640–5650. https://doi.org/10.1002/jgrc.20399

Wanninkhof, R. (1992). Relationship between wind speed and gas exchange. *Journal of Geophysical Research*, *97*(92), 7373–7382. https://doi.org/10.1029/92JC00188

Wanninkhof, R. (2014). Relationship between wind speed and gas exchange over the ocean revisited. *Limnology and Oceanography Methods*, *12*, 351–362. https://doi.org/10.4319/lom.2014.12.351

Waugh, D. W., Primeau, F., DeVries, T., & Holzer, M. (2013). Recent Changes in the Ventilation of the Southern Oceans. *Science*, *339*(6119), 568–570. http://doi.org/10.1126/science.1225411

Westberry, T., Behrenfeld, M. J., Siegel, D. A., & Boss, E. (2008). Carbon-based primary productivity modeling with vertically resolved photoacclimation. *Global Biogeochemical Cycles*, *22*, GB2024. https://doi.org/10.1029/2007GB003078

Woolf, D. K. (1997). Bubbles and their role in gas exchange. In P. S. Liss & R. A. Duce (Eds.), *The sea surface and global change* (pp. 173–206). Cambridge, UK: Cambridge University Press. https://doi.org/10.1017/CBO9780511525025.007

Woolf, D. K., & Thorpe, S. A. (1991). Bubbles and the air-sea exchange of gases in near-saturation conditions. *Journal of Marine Research*, *49*, 435–466. https://doi.org/10.1357/002224091784995765

Yang, B., Emerson, S. R., & Bushinsky, S. M. (2017). Annual net community production in the subtropical Pacific Ocean from in-situ oxygen measurements on profiling floats. *Global Biogeochemical Cycles*, *31*, 728–744. https://doi.org/10.1002/2016GB005545